UNIVERSIDAD DE CHILE
FACULTAD DE CIENCIAS FÍSICAS Y MATEMÁTICAS
DEPARTAMENTO DE FÍSICA

STUDY OF MODEL SURFACES OF MOLECULARLY FUNCTIONALIZED VANADIUM OXIDE

TESIS PARA OPTAR AL GRADO DE
MAGÍSTER EN CIENCIAS, MENCIÓN FÍSICA

JUAN CARLOS FERNÁNDEZ ARANEDA

PROFESOR GUÍA:
MARCOS FLORES CARRASCO

MIEMBROS DE LA COMISIÓN:
VICTOR FUENZALIDA ESCOBAR
RODRIGO ESPINOZA GONZÁLEZ
SAMUEL HEVIA ZAMORA

Este trabajo ha sido parcialmente financiado por Nucleo Milenio MultiMat y FONDECYT regular 1191799

SANTIAGO DE CHILE
2023

RESUMEN DE LA TESIS PARA OPTAR
AL GRADO DE MAGÍSTER EN CIENCIAS, MENCIÓN FÍSICA
POR: JUAN CARLOS FERNÁNDEZ ARANEDA
FECHA: 2023
PROF. GUÍA: MARCOS FLORES CARRASCO

ESTUDIO DE SUPERFICIES MODELO DE ÓXIDOS DE VANADIO MOLECULARMENTE FUNCIONALIZADAS

El calentamiento global es una gran amenaza para la civilización, los gases de efecto invernadero (GHGs) en la atmósfera aumentan la radiación solar absorbida, elevando la temperatura del planeta. En Chile, la industria del transporte es la mayor emisora de GHGs, por lo que es crucial cambiar a vehículos híbridos o eléctricos. Además, el uso de energías renovables puede reducir emisiones. Sin embargo, la estacionalidad de estas fuentes de energía hace necesario almacenar la energía producida durante periodos de alta producción. Por ende, las investigaciones enfocadas en mejorar la capacidad de almacenamiento de energía se han intensificado. En particular, el almacenamiento químico de energía es el más utilizado y está presente en casi todos los dispositivos electrónicos en forma de baterías recargables.
En el área de las baterías recargables, las de iones de litio (LIB) han atraído mucha atención debido a su alta densidad volumétrica y de masa para el almacenamiento de energía (400 Wh/L y 180 Wh/g respectivamente). Aunque ofrecen un diseño flexible y evitan problemas de memoria presentes en generaciones anteriores, suelen tener limitaciones en el rendimiento, las cuales están asociadas comúnmente al cátodo. Por este motivo, se exploran diversas opciones de cátodos, destacando los óxidos de metales de transición como $LiCoO_2$, $LiMn_2O_4$, $LiFePO_4$, $LiNi_0.5Mn_1.5O_4$ y V_2O_5. Entre estos, el pentóxido de vanadio destaca debido a su alta capacidad teórica de almacenamiento que llega hasta 442 mAh/g para la intercalación de tres iones Li^+ y 294 mAh/g para la intercalación de dos Li^+ por fórmula, además de su abundancia, bajo costo y fácil preparación.
A pesar de que el V_2O_5 presenta una alta capacidad de intercalación, también presenta problemas como un bajo coeficiente de difusión iónica y disolución en el electrolito, por lo cual, las investigaciones sobre interfaces electrodo-electrolito más estables se vuelven muy importantes para mejorar el desempeño del V_2O_5. A partir de los estudios de la interfaz cátodo electrolito (CEI) han aparecido algunas soluciones, entre las que destaca recubrir la superficie catódica con un material inerte reduciendo el contacto entre el electrolito y el cátodo, y regulando o promoviendo la formación de una interfaz de más estable. En este contexto, la formación de una monocapa molecular autoensamblada (SAM) en la superficie del cátodo antes del contacto con el electrolito puede ser una manera eficiente de mejorar el desempeño del V_2O_5. En este trabajo se estudió la formación de SAMs en la superficie de V_2O_5 y su influencia en el desempeño como cátodo de batería de litio. Por consiguiente, se fabricaron películas de pentóxido de vanadio de distintos espesores sobre substratos de silicio, que fueron caracterizadas química y topográficamente, luego la muestra más oxidada fue recubierta con de ácido 4-(amino)benzoico y caracterizada. Después se elaboró un nuevo conjunto de muestras sobre substratos de acero inoxidable y se funcionalizaron algunas con ácido 4-(fenilazo)benzoico (PPBA) con el fin de comparar sus propiedades como cátodo de batería. Se observó que la muestra recubierta con PPBA presenta una mayor capacidad de carga-descarga y eficiencia energética en comparación con la muestra prístina. Además de ello, el análisis postmortem apunta hacia la formación de una CEI protectora cuando se recubre con moléculas indicadas.

SUMMARY OF THE THESIS TO APPLY FOR
THE DEGREE OF MAGÍSTER EN CIENCIAS, MENCIÓN FÍSICA
BY: JUAN CARLOS FERNÁNDEZ ARANEDA
DATE: 2023
PROF. GUÍA: MARCOS FLORES CARRASCO

STUDY OF MODEL SURFACES OF MOLECULARLY FUNCTIONALIZED VANADIUM OXIDE

Global warming is one of the biggest threats to civilization, the greenhouse gases (GHGs) in the atmosphere increase the absorbed solar radiation, increasing the global temperature.
In Chile, the transport industry has the highest GHG emissions. Therefore, there is a necessity to transition to hybrid or electric vehicles. Additionally, the use of renewable energy sources to produce electricity can further reduce GHG emissions. However, the seasonality of these energy sources makes it necessary to store the energy produced during periods of high production to supply the periods of low production. As a result, research aimed at improving energy storage has been increasing. Particularly, chemical energy storage is widely used due to its presence in almost every electronic device in the form of a rechargeable battery.
In the field of rechargeable batteries, lithium-ion batteries (LIBs) have attracted a lot of attention due to their high volumetric and gravimetric energy density, reaching up to 400 Wh/L and 180 Wh/g, respectively. LIBs are also design flexible and do not suffer memory problems of first-generation Ni-based batteries. However, the performance of LIBs is primarily limited by the cathode, which often exhibits issues such as low ionic and/or electronic conductivity, dissolution in the electrolyte, and so forth. As a result, various cathode options are being studied, with transition metal oxides such as $LiCoO_2$, $LiMn_2O_4$, $LiFePO_4$, $LiNi_{0.5}Mn_{1.5}O_4$ and V_2O_5 being the most promising. Among these options, vanadium pentoxide stands out due to its high theoretical capacity (442 mAh/g for three Li^+ intercalation and 294 mAh/g for two Li^+ intercalation per formula), abundance, low cost, and ease of preparation.
Although V_2O_5 has a high theoretical capacity, it also presents problems such as a low ionic diffusion coefficient and dissolution in the electrolyte. For this reason, research on more stable electrolyte-electrode interfaces has become crucial to improve the performance of V_2O_5. Solutions have emerged from the study of cathode-electrolyte interface (CEI) such as coating the surface of the cathode with an inert material to reduce the contact of the electrode with the electrolyte and regulating or promoting the formation of a stable solid electrolyte interface (SEI) to reduce the cathode dissolution. In this context, the formation of a self-assembled monolayer (SAM) on the surface of the electrode before contact with the electrolyte can be an efficient way to improve the performance of V_2O_5.
This work studied the formation of self-assembled monolayers on the V_2O_5 surface and their influence on the cyclability as cathodes of lithium-ion batteries. Samples of vanadium oxides with different thicknesses were prepared on silicon substrates and characterized chemically and topographically. The most oxidized sample was then functionalized with 4-(amino)benzoic acid and characterized. A new set of V_2O_5 samples was prepared on stainless steel and functionalized with 4-(phenylazo)benzoic acid (PPBA). Both bare V_2O_5 and PPBA-capped V_2O_5 surfaces were characterized and tested as LIB cathodes, resulting in an increase in both the charge/discharge capacity and the energy efficiency. Furthermore, postmortem analysis indicates the formation of a protective CEI in the PPBA-capped sample.

A mi familia

Agradecimientos

Agradezco con mucho cariño a toda mi familia, con especial énfasis en mi mamá por su apoyo y cariño incondicional, a mi papi por leerme los libros del colegio y por las salidas deportivas. A mi hermanita y hermanito por brindarme tanta diversión en mis días, a mi abuela por siempre defenderme, incluso cuando el caso es indefendible, y a mi abuelo por todos los almuerzos que cocinó especialmente para mi, por ir a buscarme al colegio y comprarme algo, incluso cuando no tenía dinero, y por enseñarme a maestrear desde pequeño.
Agradezco también a Cote, por su compañía en horas de intentos de escritura y por la diversión en medio que refrescaba la mente, además de su cariño y apoyo.

Agradezco a la gama de profesores que he tenido desde pequeño, quienes me han guiado en el camino del aprendizaje y la ciencia, fomentando mi curiosidad y ayudándome a satisfacerla. En particular, a mi profesor de matemáticas de básica, "Carlos Rocky", quien detectó por primera vez mi gusto por la física. Al profesor de física, "Pesadilla", y a la profesora de química, "Brenda", en la media, quienes me impulsaron a entrar en una carrera científica. También a los profesores de la universidad que fomentaron la curiosidad científica y me enseñaron a presentar a un público, entre ellos, Marcel Clerc.

Agradezco también a los miembros y ex-miembros del laboratorio de superficies que me han guiado, acompañado y/o entablado buenas conversaciones científicas, entre ellos, Guillermo, Mackarena, Hugo, Francisca y Vicente. Además, quiero destacar a:
A Raúl Muñoz, quien me aceptó en su grupo de trabajo siendo un estudiante de primer año de especialidad, fomentando enormemente mi curiosidad por la física experimental.
A Andrés y a Víctor Fuenzalida, agradezco su iniciativa y paciencia al enseñarme a usar cada equipo que no había utilizado antes, y por confiar en mis capacidades, permitiéndome operar y, en ocasiones, incluso arreglar los diversos equipos disponibles en el laboratorio.
Y especialmente agradezco a Marcos Flores, quien además de enseñarme a usar equipos, me guió en el camino de la ciencia, fomentando enormemente las ganas de aprender. Dijo sí a estudiar cosas que me parecían interesantes y me presentó a personas que podían ayudarme a saciar mi curiosidad cada vez que era posible, creando redes que me ayudarán a formar mi camino en la ciencia.

Finalmente, agradezco también a mis amigos y amigas con quienes he compartido innumerables horas conversando, jugando o haciendo deportes, brindándome distracción en los momentos más necesarios y apoyándome incondicionalmente. Entre ellos destaco a Macka, Jo, Negrita, Feña, Guille, Norris y Eche.

Table of Content

List of Tables

List of Figures

Introduction

Global warming is one of the biggest threats to civilization. The greenhouse gases (GHGs) in the atmosphere increase the absorption of solar radiation, leading to an increase in the average global temperature [1, 2]. Some of the most relevant GHGs are carbon dioxide (CO_2), methane (CH_4), nitrogen oxides (NO_x) and chlorofluorocarbons (CFC) due to their high concentration or high global warming potential. Hence, among these gases, CO_2 is the most significant, accounting for 82% of the total GHGs and showing a strong correlation with temperature [2].

In Chile, the transport and energy industry emit the highest amount of CO_2 per year [3]. Therefore, transitioning from conventional internal combustion engine vehicles to hybrid or electric vehicles can significantly reduce CO_2 emissions [4]. Additionally, the use of renewable energy sources such as solar energy or wind power to produce electricity can further reduce CO_2 emissions, but the seasonality of these sources necessitates energy storage during periods of high production to supply the periods of low production [5].

Energy storage systems have been extensively studied, as the demand for energy storage is estimated to triple by 2030 compared to 2020 [6]. Some of these systems include pumped hydro storage, thermal energy storage, flywheel energy storage, chemical storage, among others [7]. Among them, chemical storage is the most widely used and can be found in almost every electronic device in the form of a battery. This type of system stores and releases electricity through electrochemical reactions transforming chemical energy into electricity and vice versa. Rechargeable batteries release the stored chemical energy through a reversible electrochemical process, allowing them to be recharged.

An electrochemical battery consists of an anode (a reductant), a cathode (an oxidant), and an electrolyte (which conducts cations but is an electronic insulator). For liquid electrolytes, a separator is necessary to prevent physical contact between the electrodes inside the cell. The separator must also be an electronic insulator and permeable to the electrolyte.

When a battery is being used, for example, in the discharging process, the cathode and the anode are connected outside the battery through an electronic device or a measuring device. The electrochemical potential difference between the cathode and anode induces an electron flow outside the battery. At the same time, cations in the electrolyte move, generating a concentration gradient with more cations at the cathode and fewer in the anode. This generates the chemical reactions and liberates the stored energy. When the battery is rechargeable, the charging process is stimulated by an external source, usually by applying a potential that forces cations in the electrolyte to go from the cathode to the anode either

oxidizing the cathode or reducing the anode.

Lithium-ion batteries (LIBs) are the most studied type of rechargeable battery due to their high volumetric and gravimetric energy density, reaching up to 400 Wh/L and 180 Wh/kg respectively. Figure 1 shows the comparison of energy density for different battery technologies [8]. Additionally, LIBs are flexible in design, have low self-discharge (typically $< 5\%$ per month), operate at nearly three times higher voltage than Ni-based batteries and do not suffer from the memory problem seen in Ni-Cd batteries [9].

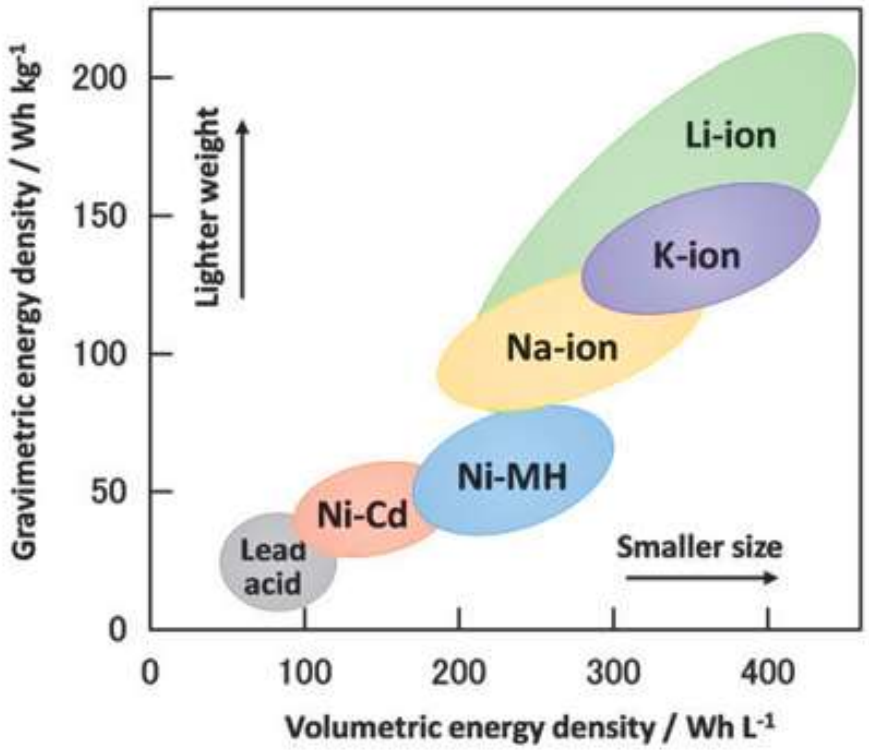

Figure 1: Comparison of mass and volume energy density of different rechargeable batteries technologies

At present, lithium-ion batteries dominate the market as a power source for portable electronic devices [10]. Additionally, their use in the hybrid and electric vehicles market is on the rise, and by 2040, the number of electric vehicles is expected to increase by a factor of 60 or 70 compared to 2016 [11]. On the other hand, LIBs have high efficiency when it comes to storing and releasing energy from sources like wind power and ocean currents, positioning them as one of the most promising contenders in the field of energy storage [12].

At present, lithium-ion batteries (LIBs) hold a dominant position in the market as the primary power source for portable electronic devices [10]. Additionally, their utilization in the hybrid and electric vehicle sector is on the rise, and projections suggest a substantial increase—possibly 60 to 70 times compared to 2016—in the number of electric vehicles by the year 2040 [11]. Conversely, lithium-ion batteries exhibit remarkable efficiency when it comes to storing and releasing energy from sources like wind power and ocean currents, positioning them as one of the most promising contenders in the field of energy storage [12].

As aforementioned, lithium-ion batteries are composed of an anode, electrolyte, and cathode. Generally, anodes are carbon or silicon-based materials, the electrolyte is usually a high concentration of lithium salt dissolved in carbon-based solvents, and cathode materials are mostly transition metal oxides or phosphates such as $LiCoO_2$, $LiMn_2O_4$, $LiFePO_4$, and V_2O_5 [9, 13]. Currently, the performance of LIBs is limited by the cathode, which exhibits small specific capacities between 160 and 200 mAh/g, compared with anode materials whose specific capacity is one order of magnitude higher, theoretically reaching up to 4200 mAh/g in the case of silicon [14]. Additionally, cathode materials have other problems such as low ionic and electronic conductivity, irreversible phase transitions, among others. For this reason, the cathode is a critical component to study to obtain LIBs with higher power and energy density.

To get a better understanding of how to enhance the cathode performance is necessary to understand how a battery works and the problems it may present. After assembling a rechargeable battery, during the first charge/discharge cycles, a spontaneous film called solid electrolytic interface (SEI) is formed on the surface of the anode due to the reduction of the electrolyte and the oxidation of the anode in the interface (see figure 2). This reaction is usually self-passivating and protects the electrode from further degradation [15, 16]. Similarly, when the operation voltage is high enough, the cathode is reduced, and the electrolyte is oxidized in the cathode-electrolyte interface (CEI), which usually does not generate a protective layer at the interface or does not produce one at all [17]. These processes are produced by the difference in chemical potential, where the anode-electrolyte interface induces an electron transfer from the anode to the electrolyte lowest unoccupied molecular orbital (LUMO), and in the cathode-electrolyte interface, it induces an electron transfer from the highest occupied molecular orbital (HOMO) of the electrolyte to the cathode [18, 19].

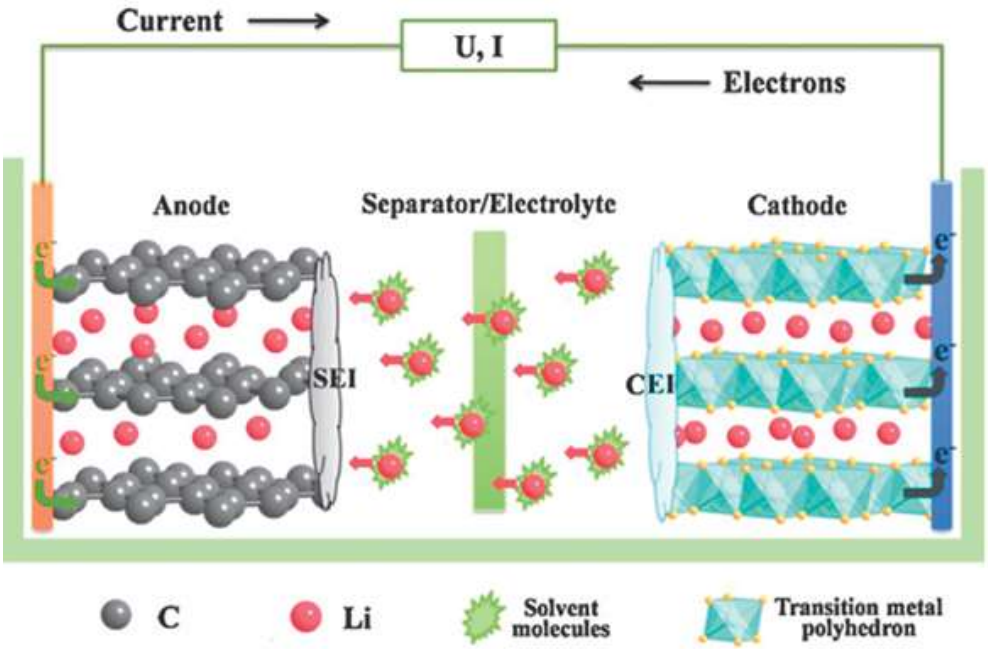

Figure 2: Battery scheme with cathode and anode, and their interfaces with electrolyte CEI and SEI respectively

In the electrolyte of the lithium-ion battery, the main components are the lithium salt and the carbon solvents. The lithium salt used, such as lithium hexafluorophosphate ($LiPF_6$), contains fluoride ions (F^-) which can release hydrogen fluoride (HF) when it reacts with trace amounts of water (H_2O) present in the system. On the other hand, the carbon solvents utilized in the electrolyte contain additional trace amounts of H_2O impurities. Consequently, when the water (H_2O) from the carbon solvent comes into contact with the lithium salt during battery operation, it initiates a reaction causing the decomposition of the lithium salt, leading to the production of more HF [20, 18, 19].

Moreover, hydrogen fluoride is highly corrosive and reacts with the lithium salt, the carbon solvents, and the cathode, leading to the deposition of new lithium salts and carbonates in the SEI and CEI [21, 22, 23, 19]. The reduction of the carbon solvent in the electrolyte produces lithium oxide (Li_2O), lithium ethylene dicarbonate (LEDC), or lithium ethylene monocarbonate (LEMC), which are the main SEI components besides ethylene, CO_2, and other products. Meanwhile, the main CEI components are oxidized carbonates and the produced lithium salts.

Additionally, HF has a preferential adsorption on the cathode surface, promoting the reduction and dissolution of the transition metal in the electrolyte, leading to the deposition of transition metal ions in the anode. These ions catalyze the electrolyte decomposition and stimulate the growth of lithium dendrites [24, 18, 19].

In cathode materials research, many efforts have been made to enhance their properties, including changing the crystal structure, doping with different elements, mixing different cathode materials, and coating the surface, among other techniques [21, 25]. These changes are intended to improve their performance in battery mode, whether it be increasing rate capability, capacity, electronic and ionic conductivity, and more. Over the past years, various cathode materials have been investigated. One of the most successful cathode materials in the commercial category was $LiCoO_2$; however, cobalt is expensive, and the structure exhibits low thermal stability and fast capacity fade. This drives the investigation of new cathode materials [25].

Furthermore, layered $LiNi_xCo_yMn_zO_2$ and $LiNi_xCo_yAl_zO_2$ (NCM and NCA respectively, with $x + y + z = 1$) have been applied in electric vehicles due to their higher capacity and thermal stability compared to normal layered compounds such as $LiNiO_2$, $LiCoO_2$, and $LiMnO_2$. Despite this, NCA, NCM, and LCO charge capacity reach up to 200 mAh/g [26, 27], making it necessary to research cathode materials with even higher capacity, such as V_2O_5, which has a theoretical capacity of 294 mAh/g when storing 2 Li ions and also possesses a layered structure [28, 29, 30, 31].

Vanadium is the fifth most abundant transition metal in the Earth's crust, found in about 65 minerals in different oxidation states, ranging from V^{+2} to V^{+5}. Vanadium can form various simple oxides, including VO, V_2O_3, VO_2, and V_2O_5, as well as more complex oxides like the Magnéli phases V_nO_{2n-1} [30] and Wadsley phases V_nO_{2n+1} [30, 32, 33]. Magnéli phases are composed of V^{+3} and V^{+4} oxidation states, starting from V_2O_3 at $n = 2$ with only V^{+3} oxidation state, and ending in VO_2 with V^{+4} when $n \to \infty$. These phases usually exhibit metal-insulator transitions at different temperatures, depending on the structure and composition, besides anisotropic charge transport, which has inspired the development of

electronic devices [30]. Vanadium Wadsley phases are quasi-layered materials composed of V^{+4} and V^{+5} oxide states, and include V_2O_5, V_3O_7, V_4O_9, V_6O_{13}, and the B phase VO_2 [32, 30]. These compounds are suitable for electrochemical devices, thanks to their stable layered structure with the ability to reversibly intercalate ions [32]. Particularly, V_2O_5 is the most stable oxide and has been extensively studied due to its physical properties, such as electrochromism, field-emission, and electrochemical properties, leading to many applications, including sensors, electrochromic windows, catalysts, actuators, among others.

Interest in vanadium pentoxide as a cathode material has recently increased due to the resurgence of lithium metal as an anode for LIBs, which eliminates the biggest obstacle of vanadium pentoxide - its lack of inherent lithium ions. Moreover, V_2O_5 proves to be a promising candidate not only for lithium-ion batteries (LIBs) but also for other metal batteries like sodium-ion batteries and magnesium-ion batteries [13]. Additionally, it is easy to obtain nanostructures of vanadium pentoxide, such as nanofibers, nanobelts, nanorods, and more [34].

Another advantage of vanadium pentoxide is its abundant sources, low cost, ease of preparation, and good safety characteristics compared to other cathodes used in LIBs. Furthermore, V_2O_5 has the ability to store two lithium ions with a theoretical capacity of 294 mAh/g, which is higher than that of typical layered compounds. These factors make vanadium a highly promising material for lithium storage.

Vanadium pentoxide is a typical intercalation compound and has eleven possible structures, among which the most stable is the orthorhombic layered structure with the $Pmnm$ symmetry with lattice parameters $a = 11.512$ Å, $b = 3.564$ Å, and $c = 4.368$ Å, where the layers are held together by weak Van der Waals forces in the c direction. Furthermore, a complete unit cell is comprised of two formula units, and the structure is made out of VO_5 square pyramids with the vanadium in the center surrounded by oxygen. The pyramid shares edge and corner with the adjacent pyramids forming a double chain linked along the a axis forming a layered structure with a distorted close-packed oxygen array. The structure of V_2O_5 promotes the ion intercalation between the layers rather than through them [31], distorting the lattice as ions intercalate, leading to phase transitions.

Depending on the lithium intercalation degree (x in $Li_xV_2O_5$), we can observe different phase transitions in V_2O_5. Some of these phases are labeled as α, ε, δ, γ, and ω. These phase transitions manifest in the charge or discharge profile as distinct plateaus. Specifically, the α-ε, ε-δ, δ-γ, and γ-ω transitions occur at 3.4 V, 3.2 V, 2.2 V, and 1.9 V, respectively, and induce volume changes (refer to figure 3 [35]). The first phase, α-$Li_xV_2O_5$, has the minor lithium concentration ($x < 0.1$), and the structure of pristine V_2O_5 slightly changes. Then, with increasing lithium content, the $Li_xV_2O_5$ structure starts puckering, changing to ε-$Li_xV_2O_5$ ($0.35 < x < 0.7$), and δ-$Li_xV_2O_5$ ($0.7 < x <= 1$), with an increase in volume near 11%. These phase changes are fully reversible when lithium is inserted and extracted from the structure in the voltage range $2.4 - 4.0$ V. When more lithium is inserted and $x > 1$, a structural change from δ-$Li_xV_2O_5$ to γ-$Li_xV_2O_5$ phase occurs through the rotation of two VO_5 square pyramids in opposite directions giving way to a puckered chain of square pyramids that alternate up and down. This δ-γ phase transition is irreversible and involves a relative volume contraction of $\sim$7%. Moreover, γ-$Li_xV_2O_5$ itself can reversibly intercalate

Li-ions in the range $0 < x \leq 2$ in the $2-4$ V range, reaching the highest reversible capacity of 294 mAh/g. Deeper discharge of γ-$Li_xV_2O_5$ leads irreversibly to the formation of ω-$Li_xV_2O_5$ phase, which allows storing up to 3 Li-ions. Further study of this phase indicates that after the first discharge-charge process, 0.4 mol of Li gets trapped, and then in the second discharge, 2.65 mol gets trapped, indicating that the ω-$Li_xV_2O_5$ phase is irreversible [36].

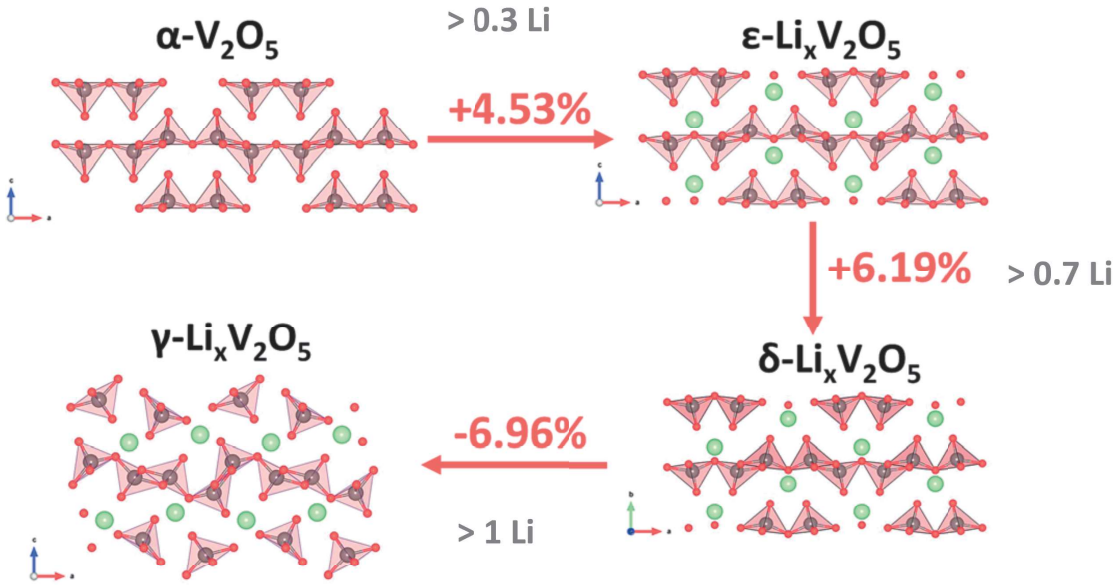

Figure 3: Crystal structure and volume change during lithium intercalation in V_2O_5

Although V_2O_5 has high capacity, it may present some problems, such as low lithium-ion conductivity, moderate electric conductivity, and poor cycling stability, causing low reversible capacity at large current densities. Many efforts have been made to enhance ionic and electronic conductivity and structural stability of vanadium pentoxide cathodes for LIBs. Among the most studied strategies, the construction of nanostructured V_2O_5 allows for an increase in the surface area of de/intercalation and shortens the diffusion path length for ions and electrons. Cation doping can improve the electrical conductivity and cycling stability by reducing polarization [29].

Another strategy to enhance the cathode performance is coating its surface with a suitable material, such as ion and electron conducting polymers, carbon-based structures, or other materials that can protect the cathode from dissolution by avoiding contact with the electrolyte[29]. Also, one way to induce the formation of a protective coating is by adding additives in the electrolyte, enhancing the interfacial stability due to the additive decomposition prior to solvent oxidation [37]. For instance, Zhuang et al. [38] studied para-aminobenzoic acid (PABA) as an additive in the electrolyte and showed that PABA molecules are adsorbed on the cathode surface, improving the capacity retention from 61 to 94%. A more recently studied alternative to protect the cathode from the electrolyte, also with high thickness control, is to cover the cathode's surface with Self-Assembled Monolayers (SAMs)[37]. SAMs can form a homogeneous ultrathin and dense layer. Besides, SAMs are both mechanically and chemically stable due to their strong immobilization on the oxide surface through the formation of chemical bonds and can be highly ordered, supported by intermolecular interactions [39]. Thus, it is known that SAMs can change the chemical and physical properties

of solid surfaces [39, 37].

Motivated by the above, the main objective of this work is to investigate the influence of functionalization with molecules onto vanadium oxides' surfaces on the cyclability in lithium-ion batteries. The samples are topographically characterized by atomic force microscopy (AFM) in contact mode and electrically by conductive AFM. Also the chemical composition and oxidation states are obtained by X-ray photoelectron spectroscopy (XPS), and angle-resolved XPS is used to prove the adhesion of the molecules.

This work was financed by Nucleo Milenio MultiMat and by the project fondecyt regular 1191799

Chapter 1

Experimental Section

In this chapter, the experimental techniques used to characterize the samples are described. The methods used to elaborate the vanadium pentoxide, deposit the molecules on the surface, assemble and test the batteries are also explained. Finally, the methods used to characterize the samples are presented.

1.1 Experimental Techniques

The experimental techniques and equipment used in this work are mentioned and described in the following sections. We will start with the techniques used to elaborate the samples, followed by the description of the equipment used to characterize them.

1.1.1 Electron beam evaporation

This is a physical vapor deposition (PVD) technique in which an electron beam collides with the material to evaporate, contained in a crucible. The electron beam is generated by passing a current through a filament using thermionic emission. The electrons' trajectories are curved by a magnetic field and a beamformer while being accelerated by a high voltage, directing them towards the crucible. As the electrons hit the surface of the material, it heats up, increasing the vapor pressure until the desired evaporation rate is achieved.

The evaporated material is expelled radially, covering everything in the vacuum chamber, including the substrate. This equipment allows precise control of the electron emission current and the acceleration potential applied, thereby enabling accurate regulation of the evaporation rate (see figure 1.1).

1.1.2 Quartz tube furnace

This is a hermetic quartz tube usually surrounded by heating coils in a thermally insulating matrix with the capacity to maintain a controlled atmosphere and control the temperature via feedback from a thermocouple. This is usually used to promote different chemical reactions at the surface of the substrate with different reagents. In figure 1.2 the quartz tube furnace

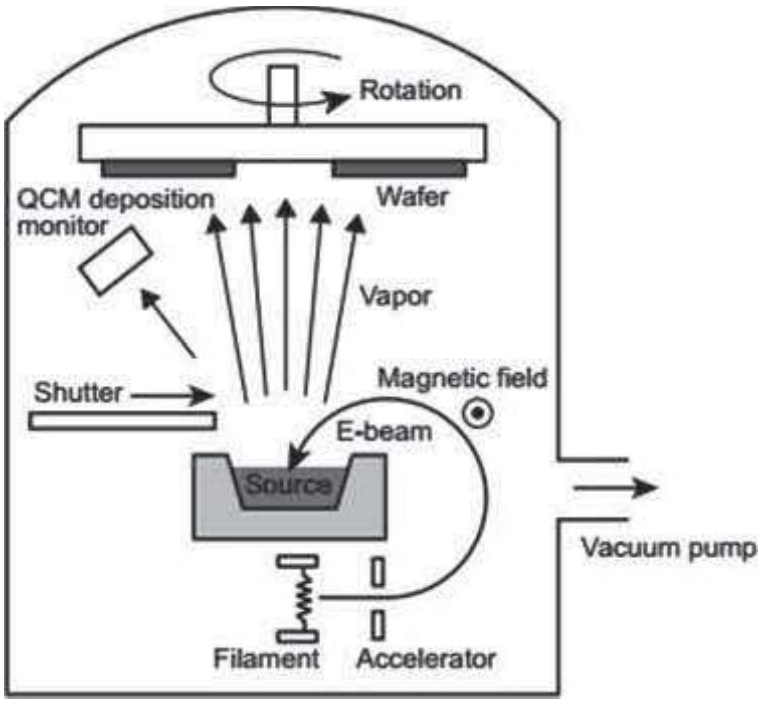

Figure 1.1: Operation diagram of an electron beam evaporation system

used is shown in the left panel, and the flow controllers are shown in the right panel.

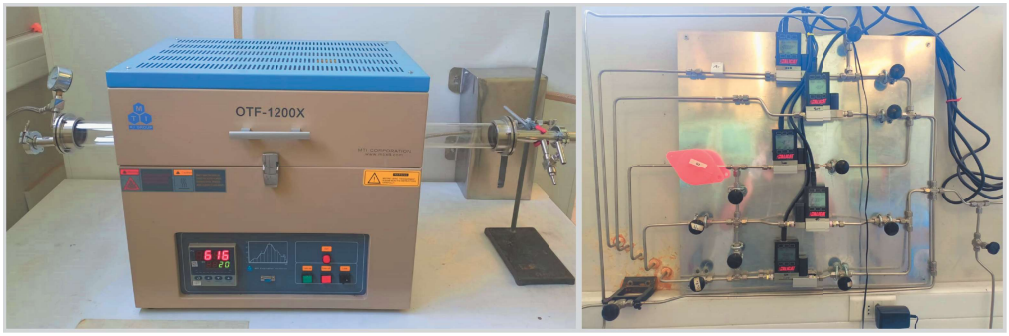

Figure 1.2: Real images of the quartz tube furnace used and its flow controllers in Physics Department at PUC.

1.1.3 Scanning electron microscopy

The Scanning Electron Microscope (SEM) is a research tool that utilizes an electron beam instead of visible light to capture high-resolution images at the microscopic and nanometric levels. The SEM operates by generating a high-energy electron beam, which is focused and scanned across the surface of the sample. When these electrons interact with the sample, secondary signals, such as secondary electrons (SE) and backscattered electrons (BSE), are produced, providing detailed information about the sample's topography, composition, and structure. Additionally, the SEM is capable of conducting chemical analyses and particle size measurements using advanced techniques such as energy-dispersive X-ray spectroscopy (EDS). See figure 1.3[40]

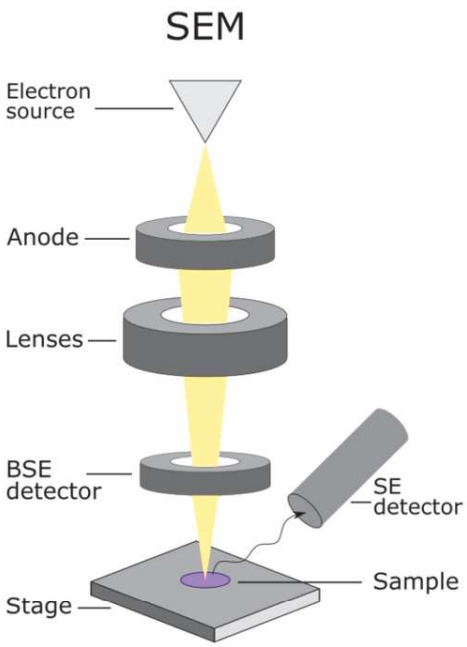

Figure 1.3: Schematic diagram of Scanning Electron Microscope

1.1.4 X-ray photoelectron spectroscopy

The X-ray photoelectron spectroscopy is a technique used to study the chemical composition of the surface of a material. In this technique, the surface to be analyzed is irradiated by an X-ray source, causing the emission of electrons (photoelectrons) due to the photoelectric effect. These electrons are directed to a detector where their kinetic energy is measured, and it is given by the equation 1.1 [41].

$$E_k = h\nu - E_B - \phi \tag{1.1}$$

where $h\nu$ is the energy of the X-ray photons, E_B is the binding energy of the electrons, which depends on the atomic orbital from which the electron comes, and ϕ is the spectrometer work function (see figure 1.4 [42]).

Since the binding energy depends on the atomic species and its orbital, each element has a different spectrum, which allows for their identification. Also, a change in the oxidation state yields a shift in the binding energy, which allows us to glimpse the oxidation state of the element in question. Therefore, as the photons' energy is a fixed variable, dependent on the anode used to generate the X-ray, which are usually Al (Kα = 1486.6 eV) or Mg (Kα = 1253.6 eV), and the work function is a parameter dependent on the spectrometer, it is enough to measure the photoelectrons' energy to determine the elemental composition.

1.1.5 Atomic force microscopy

This is a type of scanning probe microscopy technique that utilizes a cantilever with a sharp tip fixed at the end. The back of the cantilever is reflective, and a laser light is directed onto its back during operation and reflected to a detector. While the tip "touches" the surface

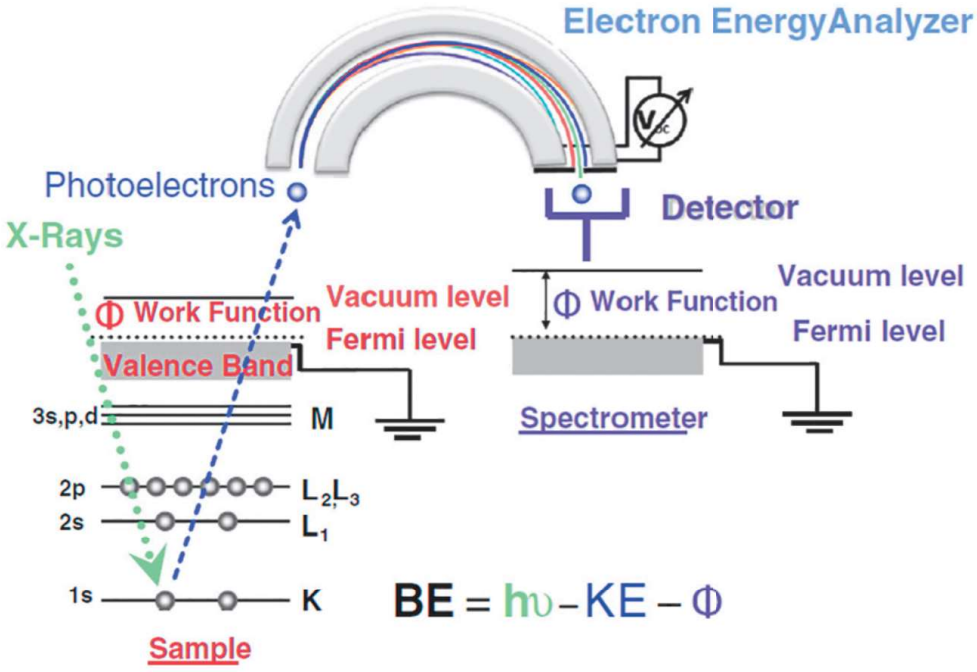

Figure 1.4: Representation of the photoelectric effect in an XPS system

being analyzed, the deflection and motion of the cantilever are detected and recorded with the detector.

Usually, the detection system consists of a laser light from a solid-state diode, which is deflected on the back of the cantilever and directed towards a position-sensitive photodetector. This allows us to identify vertical and horizontal deflections by analyzing the relative intensities (see figure 1.5). As a result, we can measure the interaction force between the tip and sample, which is well described by a $Lennard - Jones$ potential (see figure 1.6). Consequently, we can establish a relationship between the measured interaction force and the height differences, obtaining a topographic image.

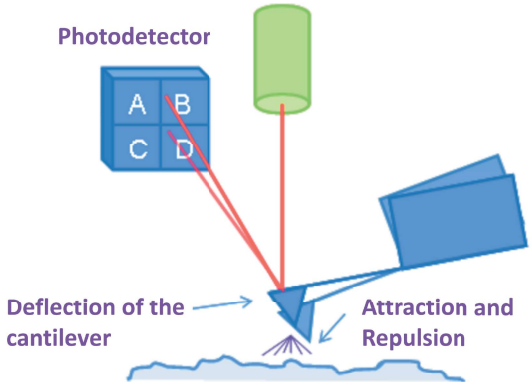

Figure 1.5: Herein presents a schematic representation of the operation of an Atomic Force Microscope (AFM).

1. Contact mode: In this measurement mode, the tip is in the repulsive region of the

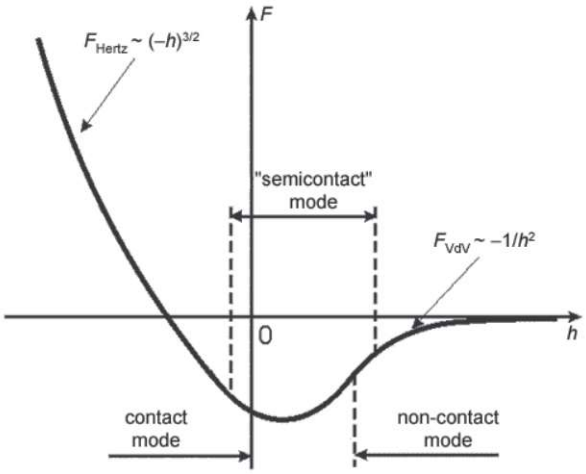

Figure 1.6: Operating mode of AFM according to the potential region.

potential, which is defined as physical contact. The tip is dragged across the sample, and the surface is contoured by either using a constant distance or constant force repulsion between the tip and the sample. This scanning mode allows for better imaging but causes more erosion on the tip

2. Non-contact mode: Here, the tip and sample are in the attractive region of the potential, and the cantilever-tip system is oscillating at its natural frequency. As the tip sweeps the sample, the tip encounters valleys and peaks, which change the tip's distance to the surface; therefore, the oscillation frequency changes. This change is detected by the photodetector, and by applying feedback, the tip is repositioned, and the displacement is recorded. Since the tip is far from the sample, the lifespan is higher, but the lateral resolution decreases.
3. Tapping mode: In this operating mode, the tip is driven to oscillate, maintaining a constant amplitude, going through the attractive and repulsive parts of the potential (That is why this mode is also known as semi-contact mode). Then, the amplitude of the cantilever's oscillation changes when approaching a valley or peak; this change is detected, and the tip is repositioned, obtaining the topographic image. This mode grants better lateral resolution than non-contact mode and a higher lifespan than contact mode.

In contact mode, there is also the option to apply a bias voltage between the tip and the sample, which allows getting current images and voltage-current curves for specific points or areas of the sample while sweeping it. To obtain this current, it is necessary to use a conductive tip, which is usually made by coating the tip with a conductive material. This application is called conductive AFM (C-AFM).

1.1.6 Galvanostat and Potentiostat

These electrochemical techniques consist of varying the voltage of an electrochemical cell within a certain range of interest. As the potential is varied, the cathode undergoes reduction or oxidation, going through phase transitions.

In a galvanostat, the voltage is varied by applying a constant current through the elec-

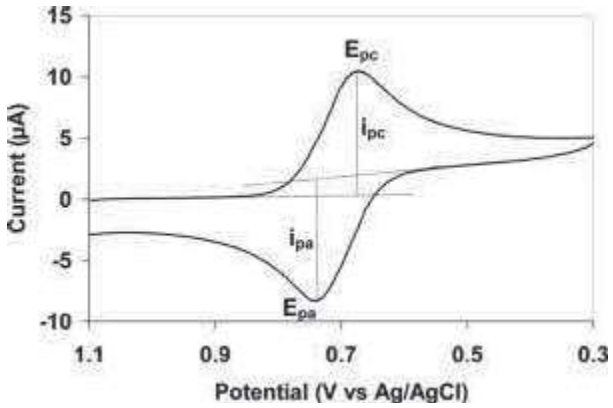

Figure 1.7: Typical cyclic voltammetry diagram in a charge/discharge process

trodes, which allows the calculation of charge/discharge capacity using the formula $Q = I \times t$, where I is the applied current and t is the charge/discharge time. Cyclability measurements are made by charging and discharging at a constant current, and rate capability is measured by charging and discharging at different currents.

The potentiostat is an electronic device that maintains the potential of an electrode with respect to another by adjusting the current. This equipment allows for performing cyclic voltammetry, a technique used to sweep the selected potential window by changing the potential linearly and collecting the current densities as a function of the potential. This allows the observation of current peaks, which appear at the potential where redox reactions take place (see figure 1.7).

1.2 Samples' preparation

Vanadium pentoxide thin films were fabricated by the group of professor Samuel Hevia at the institute of physics at the Pontificia Universidad Católica de Chile. The samples were prepared on two different substrates: n and p doped Si(100) (1 to 10 Ωcm) and polished stainless steel (SS) AISI 304. Before the evaporation, the SS coins were washed and polished with sandpaper, followed by a two-step polish with alumina suspensions and distilled water. First, using a particle size of 0.3 μm, and then with alumina suspension of 0.05 μm particle size.

For the vanadium pentoxide, first, metallic vanadium thin films were evaporated by electron-beam from vanadium pellets (99.8% purity). The deposition was performed in high vacuum with a base pressure of 10^{-7} mbar, and the pressure during the deposition was kept below 2×10^{-6} mbar. The evaporation rate and the final thickness were measured during the process. The evaporation rate was 6 nm/min and remained constant throughout the evaporation. The thicknesses of metallic vanadium films achieved were 10, 25, 50, 100, and 150 nm.

After the evaporation, the vanadium films were oxidized following this protocol: First, a horizontal quartz tube furnace was purged with 200 sccm of Ar flow at room temperature. Then, Ar flow was turned off, and O_2 was introduced with a flow of 200 sccm along with the

start of a temperature gradient. After 30 minutes, the system reached 500 °C, and the system was maintained under these conditions for 60 min. Finally, the heater source was turned off, and the O_2 flow was maintained until the quartz tube returned to room temperature. The resulting thicknesses obtained were 30 ± 1, 75 ± 3, 150 ± 5, 300 ± 10 and 450 ± 15 nm. These thicknesses were measured by atomic force microscopy on samples with a clean edge prepared through lithography, and by scanning electron microscopy cross sections images of vanadium pentoxide (see ref. [31]).

The samples functionalized with molecules were prepared by immersing the vanadium oxide thin films in a solution of molecules in 2-propanol at a concentration of $C = 10\ mM$. The para-aminobenzoic acid ($H_2NC_6H_4CO_2H$) samples were immersed for 20 hours, while the para-(phenilazo)benzoic acid ($C_6H_5N = NC_6H_4CO_2H$) samples were immersed for 24 hours. After the immersion, the samples were washed with 2-propanol and dried under a flow of N_2.

To prepare the samples for measurement in battery mode, the vanadium oxide cathodes were transferred to a glove box in an argon atmosphere where they were assembled as the cathode of the lithium battery. The battery assembly involved using a Swagelok PFA straight union of 1/2 inches with stainless steel 304 collectors. First, lithium metal was attached to one end of the battery as the anode, and then the fiberglass separator was placed on top of it. Next, drops of lithium hexafluorophosphate electrolyte were added until the separator was moistened. Finally, the cathode was placed on top of these components to close the cell.

1.3 Samples' Characterization

To identify the topography, chemical composition, and battery performance of the vanadium oxide samples, the following procedures were followed.

1.3.1 Chemical characterization

To identify the chemical composition and oxidation states, an XPS equipment with angle-resolving capabilities was used. The analysis started with a wide spectrum to identify the atomic species present on the sample. Subsequently, high-resolution spectra were obtained for the species of interest to analyze their oxidation states.

For the PPBA powder, a high-resolution spectrum was obtained to infer the oxidation states of carbon in the material and their associated binding energy. The same analysis was performed for nitrogen and oxygen spectra.

Regarding the vanadium oxide samples, high-resolution spectra of vanadium and oxygen were measured to determine the initial oxidation states of the sample. These spectra were then compared with the spectra of the functionalized samples. Additionally, signals of carbon and nitrogen were analyzed to confirm the presence of the molecule. Furthermore, angle-resolved XPS was performed at different angles to gain insight into the orientation of the molecules.

1.3.2 Topographic and electrical characterization

AFM (Atomic Force Microscopy) and C-AFM (Conductive Atomic Force Microscopy) equipment were employed to gather information on the topography and electrical properties of the samples. Topographical images were taken for both the bare V_2O_5 and the V_2O_5 samples capped with molecules. These images were obtained at a size of 5000×5000 nm^2, allowing the determination of surface roughness, and smaller images were also captured enabling observation of smaller structures. Subsequently, conductive AFM was utilized to electrically characterize these structures.

1.3.3 Cyclic Voltametry

The samples were pre-lithiated in a IviumStat.h standard ($\pm$ 5 A /$\pm$ 10 V) using cyclic voltammetry (CV) at a to ensure an identical starting point and to obtain the position of redox peaks. The CV was performed in the voltage ranges of $2.6-4$ V and $2-4$ V, at a scan rate of 0.1 mV/s. The potential resolution of this instrument is 0.02 mV, with an accuracy of 0.2% or 1 mV.

1.3.4 Cyclability

For the battery mode test, a technique is used to vary the voltage of the electrochemical cell by applying a constant current, which charges or discharges the battery within the range of interest. In the case of the vanadium pentoxide cathode, the voltage range is from 2 to 4 V, where 2 atoms of lithium are inserted into the vanadium pentoxide structure ($2 > x > 0$ in $Li_xV_2O_5$). The batteries were tested using a BT2143 potentiostat/galvanostat system from Arbin Instruments. First, the battery is discharged from its starting voltage at 0.1C to obtain a common starting voltage for all samples. Then, one cycle is performed at 0.1C, followed by 100 cycles at 1C. [1]

[1]Battery C-rate is a standardized measure representing the rate at which a battery is charged or discharged relative to its nominal capacity. It is expressed as a multiple of the battery's capacity. For instance, a 1C rate indicates the battery can be fully charged or discharged in one hour, while a 0.5C rate would take two hours for a complete charge or discharge.

Chapter 2

Study of bare vanadium pentoxide surface

The bare surfaces of vanadium pentoxide (V_2O_5) with different thicknesses, which were elaborated using the previously described method, were studied using several techniques, including SEM, AFM, XPS, and AR-XPS. These techniques allowed for the characterization of their surface topography and chemical composition.

2.1 Topographic characterization

The samples to analyse are of different thicknesses. Those are 30 ± 1, 75 ± 3, 150 ± 5, 300 ± 10 and 450 ± 15 nm, measured by means of atomic force microscopy (AFM) and scanning electron microscopy (SEM). Therefore, those techniques were also used to identify the topographic structures and analyze the surface.

Scanning Electron Microscope (SEM) images of vanadium pentoxide samples on stainless steel were captured to initially assess the surface appearance. In figure 2.1, the nanostructuring of the surfaces is evident. For the 30 nm thickness (a), elongated structures are observed in various directions. For the 75 nm thickness (b), the surface configuration bears a resemblance to a disk-like shape [43], appearing to lie in-plane over the substrate. As the thickness increases from 150 nm to 450 nm, disk-shaped structures are observed in all directions. It appears that in the 30 nm and 75 nm thicknesses, the structures do not completely cover the substrate, and the Si signal from the substrate is detected in XPS, as will be discussed in subsequent sections. Furthermore, the surface microstructure in all samples is homogeneous regardless of the thickness, allowing observation by AFM in contact mode.

The AFM topographic images of bare V_2O_5 samples show high surface roughness in all thicknesses due to the formation of structures. The highest surface roughness is observed in the sample with a thickness of 30 nm, reaching up to 45 nm RMS. This sample also presents a different kind of structures compared to the samples of higher thicknesses, which appear similar to nanobelts, see in figure 2.2a and 2.2b [44, 45].

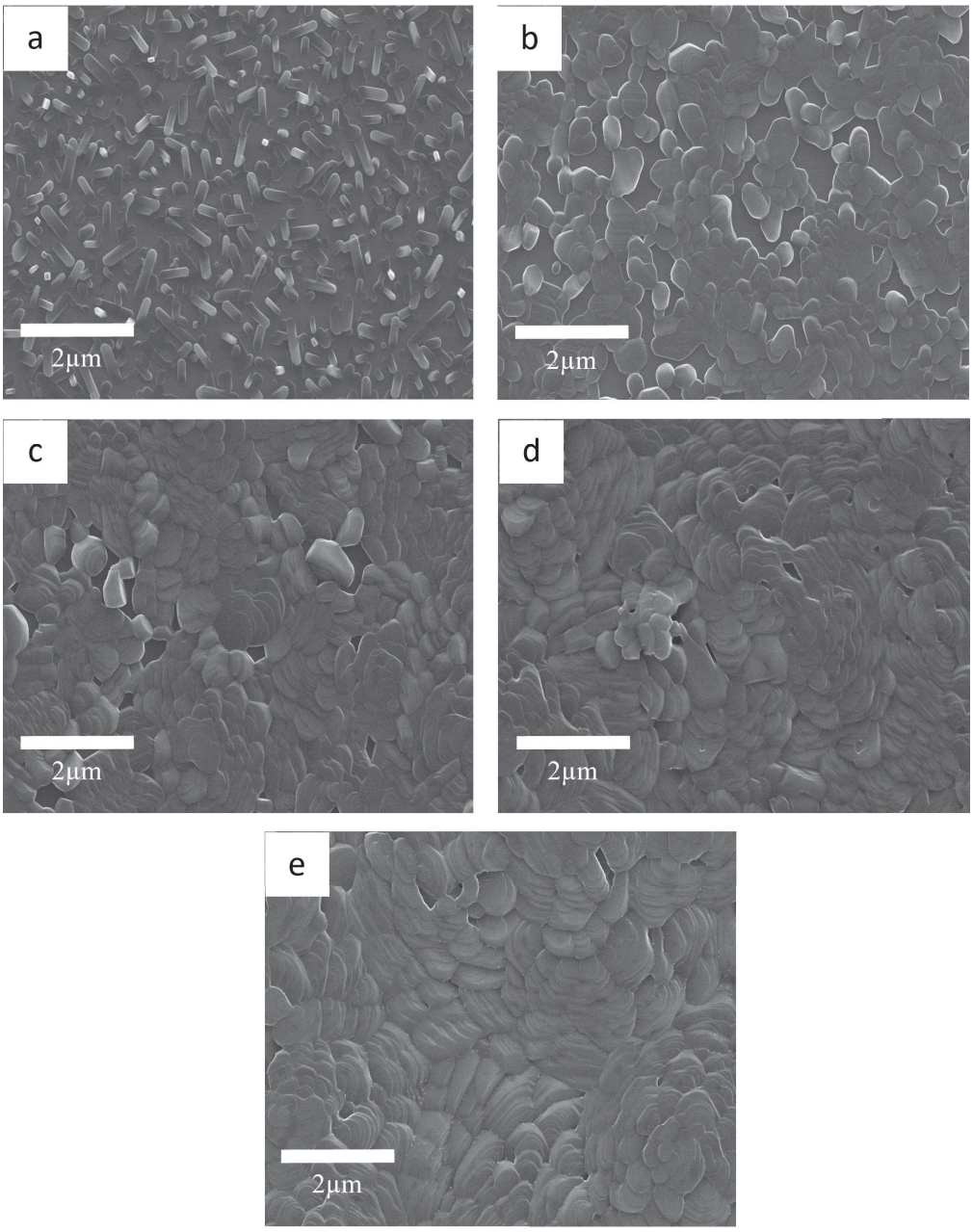

Figure 2.1: SEM images of different vanadium oxide thicknesses a) 30 nm, b) 75 nm, c) 150 nm, d) 300 nm, e) 450 nm.

At larger thicknesses, the structures change to disk-like sheets (see figure 2.2(c-f)), reducing the RMS roughness. Thus, the 75 nm sample shows the smallest roughness ($RMS < 30$ nm) associated with the disk-shaped structures oriented in-plane; this value increases to 40 nm in the 150 nm sample and decreases at higher thicknesses (see figure 2.2(g)). The lower roughness of the 75 nm sample and the increase in the 150 nm sample are attributed to an increase in the coverage of the substrate.

The disk-like sheets present both terraces and borders, where the terraces are atomically flat, mainly oriented at the [001] direction, with an RMS roughness of 0.5 nm. This topogra-

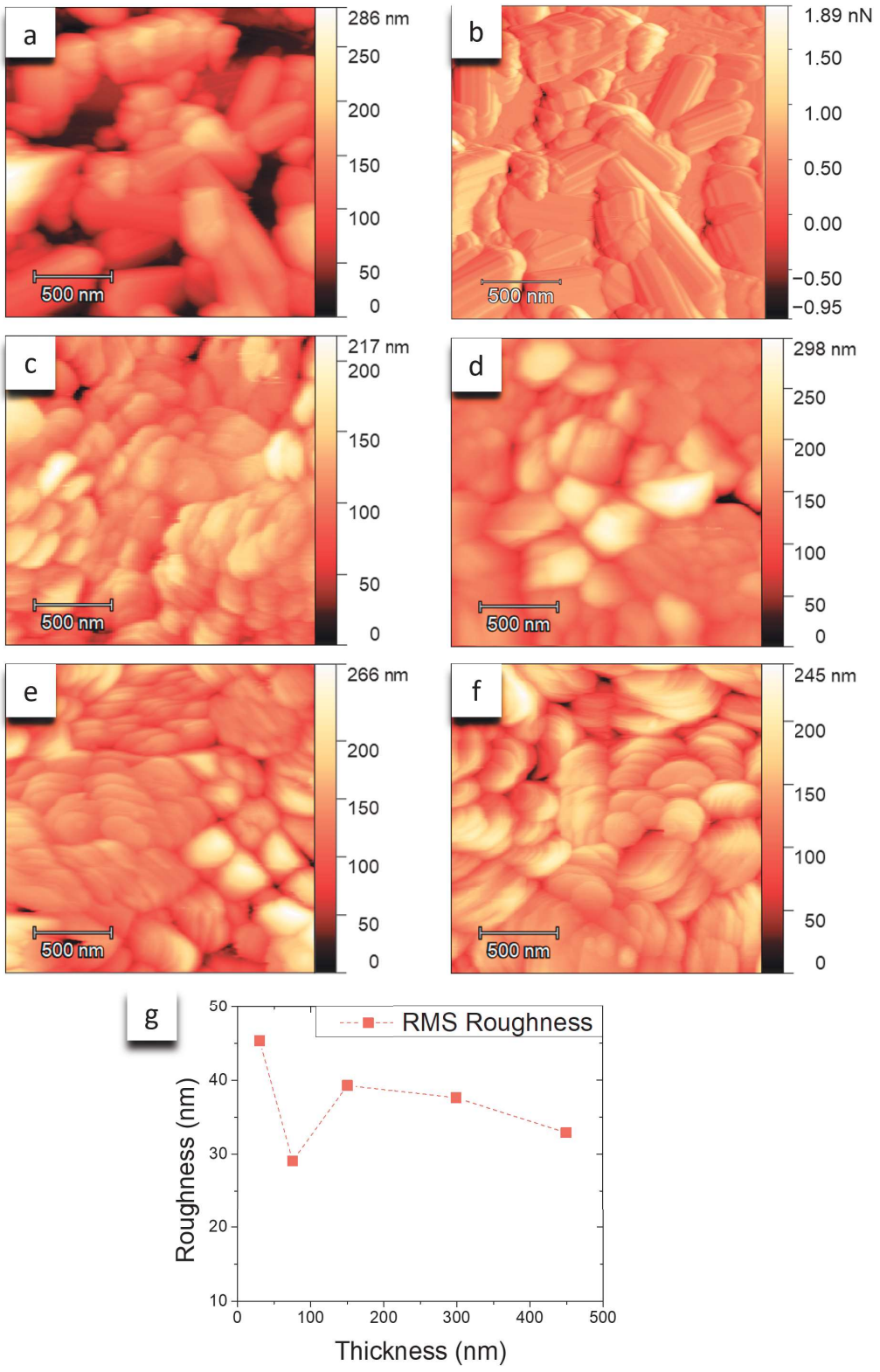

Figure 2.2: AFM images of V_2O_5 samples with varying thicknesses: a) Topography and b) Normal force for 30 nm thickness; Topography for c) 75 nm, d) 150 nm, e) 300 nm, and f) 450 nm thicknesses; g) Evolution of RMS roughness with thickness.

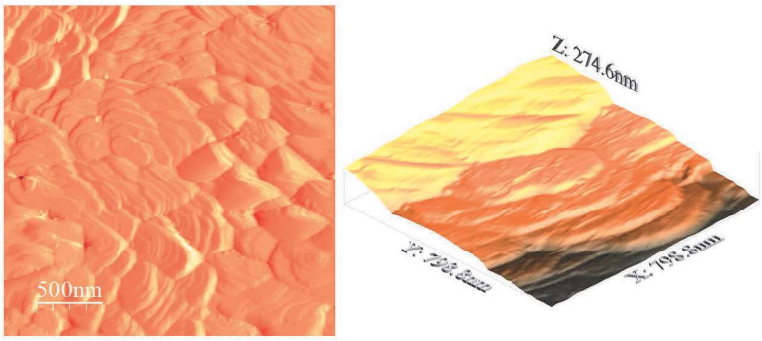

Figure 2.3: AFM topographic images of V_2O_5 displayed in 2D of 2000×2000 nm^2 and zoom in from a terrace in 3D.

phy is typical of layered materials [43]. Furthermore, the largest terraces were found in the sample of 300 nm thickness, covering areas of several 10^{-1} μm^2 (see figure 2.3).

2.2 Chemical characterization

The chemical characterization was performed by XPS, and first, a spectrum with a broad energy range (1200 eV - 0 eV in binding energy) was obtained at a measurement angle set at 65 degrees with respect to the horizontal. The signals related to oxygen, vanadium, nitrogen, and carbon species were identified in all thicknesses (see figure 2.4).

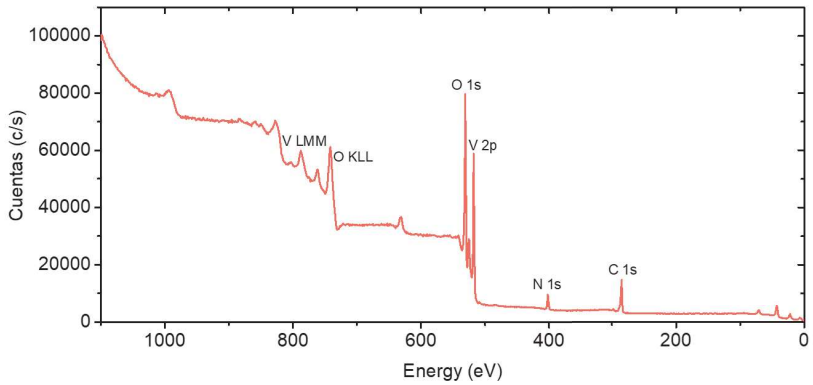

Figure 2.4: XPS spectrum of the 300 nm sample in a broad energy range (1200 eV - 0 eV, binding energy) at a take-off angle of 65°, showing signals related to oxygen, vanadium, nitrogen, and carbon species.

From high-resolution XPS (HR-XPS), the adventitious carbon signals $C-C/C-H$, $C-OH/C-O-C$, and $C=O$ were found at 284.6 eV, 286.2 eV, and 288.3 eV, respectively. Additionally, nitrogen peaks associated with adsorbed nitrogen onto vanadium oxides [46] were identified, and these were fitted with two peaks at 399.7 eV and 401.6 eV. See figure 2.5

(a) and (b).

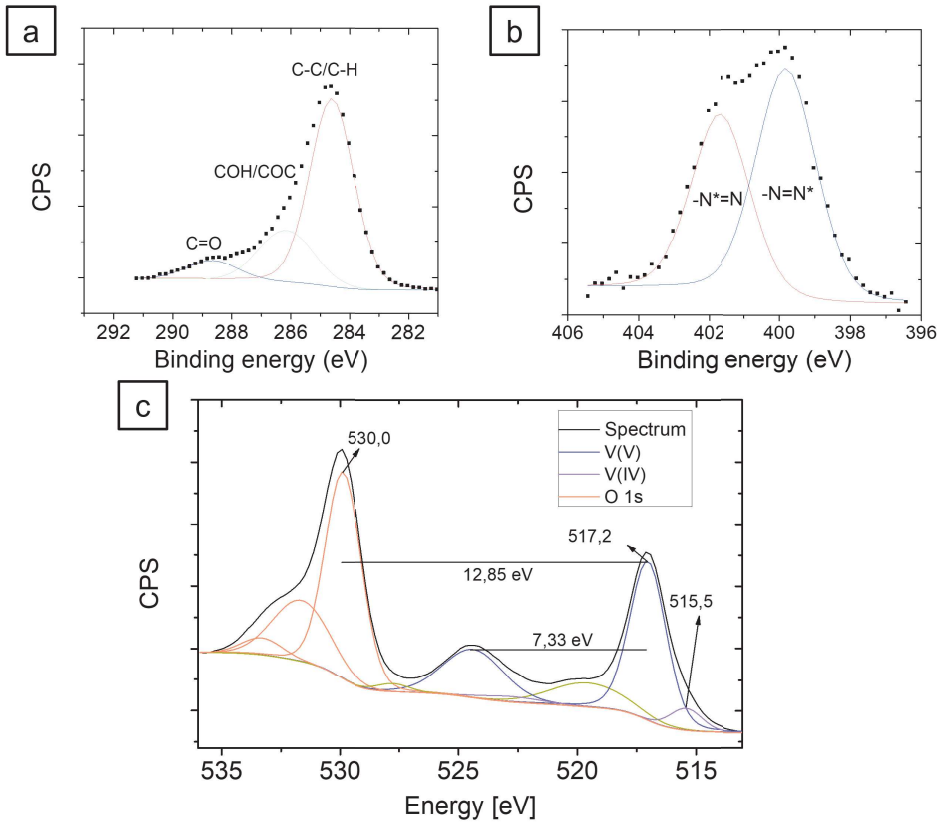

Figure 2.5: High-resolution XPS spectra reveal various signals: a) adventitious carbon signals $C-C/C-H$, $C-OH/C-O-C$, and $C=O$, b) nitrogen peaks at 399.7 eV and 401.6 eV attributed to adsorbed nitrogen onto vanadium oxides and c) the combined spectrum of vanadium V2p and oxygen O1s, with $O1s-V2p_{3/2}$ and $V2P_{1/2}$-$V2P_{3/2}$ distances with O1s reference.

Furthermore, in the combined spectrum of vanadium $V2p$ and oxygen $O1s$, two or three peaks are observed in the oxygen's side spectrum, accompanied by four peaks attributed to vanadium and an additional two peaks corresponding to satellites on the vanadium side, as reported in [47]. This observation suggests the presence of three oxygen bonds and two vanadium oxide states, as illustrated in Figure 2.5 (c).

The two oxygen peaks are identified as O^*-V bond, located at 530.0 eV and the $V-O^*H$ bond, found at 531.7 eV. As shown by Mendialdua et al. [48], the best binding energy reference for vanadium oxides is the peak of the oxygen associated with the vanadium bond (O^*-V), which has also been reported by many authors [48, 28, 49, 43]. This difference in binding energy between the oxygen and vanadium core levels, $\Delta_{OV}=O1s-V2p_{3/2}$, allows for the correct identification of the oxidation state of vanadium.

In this regard, the peaks obtained for vanadium at 517.2 eV and 515.5 eV were identified as V^{+5} and V^{+4} oxide states, respectively, with $\Delta_{OV^{+5}}=12.8$ eV and $\Delta_{OV^{+4}}=14.5$ eV. Additionally, there is no agreement on the energetic distance between $V2p_{3/2}$ and $V2p_{1/2}$ peaks, and in this work, it was found to be 7.33 eV. See figure 2.5 (c).

By comparing the equivalent homogeneous atomic fraction XPS atomic composition for different thicknesses, as displayed in Table 2.1, we observed the Si spectra from the substrate, which remains present until a thickness of 150 nm is reached. Beyond that point, the signal disappears, attributed to substrate coverage, as mentioned earlier. Additionally, nitrogen and adventitious carbon signals were present in all spectra.

Thickness [nm]	Vanadium	Oxygen	Carbon	Nitrogen	others
30	7.1	53.7	25.0	2.0	12.2
75	12.5	47.8	33.2	2.4	4.1
150	14.9	49.2	29.3	2.6	4.0
300	22.8	60.2	16.0	1.0	0.0
450	16.6	51.9	29.3	2.2	0.0

Table 2.1: Percentage of atomic concentration by specie and thickness

The atomic composition is summarized in table 2.1, and it can be seen that the sample of 300 nm has the highest vanadium composition. Moreover, through HR-XPS, it is observed that this sample also has the highest proportion of V^{+5} oxidation state (see figure 2.6). This proportion agrees with the lower nitrogen content, which is expected to decrease when increasing V^{+5} proportion, due to the high affinity of nitrogen with V^{+4} sites rather than V^{+5} [46]. The ratio $V^{+5} : V^{+4}$ of vanadium is close to 15, and the nitrogen content is close to 1%.[46].

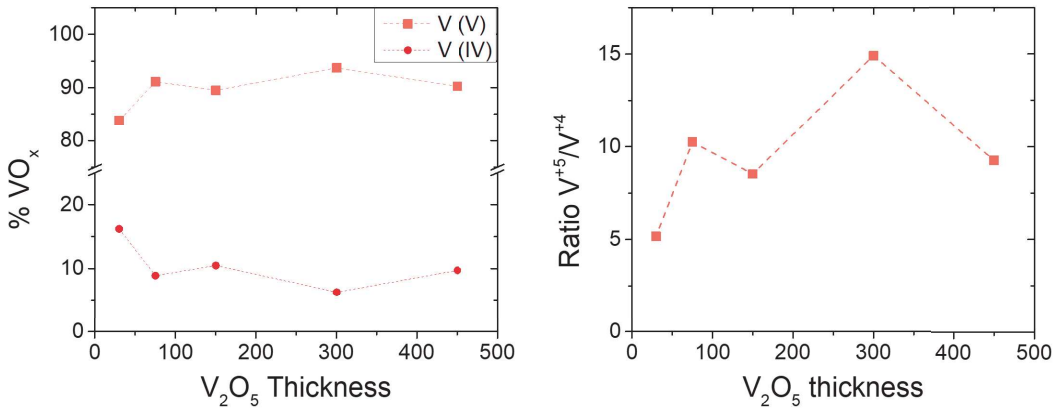

Figure 2.6: a) Vanadium V^{+5} and V^{+4} percentage and b) vanadium V^{+5}/V^{+4}

Chapter 3

Study of para-aminobenzoic acid onto vanadium pentoxide surface

The sample chosen to be functionalized with PABA was the 300 nm thick one due to its chemistry and topography, which marked it as the best choice for attaching molecules because of its extensive terrace areas and high oxidation state, in a proportion $V^{+5} : V^{+4} = 15 : 1$. Additionally, this sample also exhibits a lower concentration of adsorbed nitrogen. Therefore, this chapter presents the characterization of PABA SAM on vanadium pentoxide, using AFM and XPS, and compares it with the bare surface.

3.1 Topographic characterization

The AFM topographic images of PABA-coated V_2O_5 show the same structures as before deposition, as expected, and high surface roughness (RMS = 32.1 nm), which remains unchanged compared to the bare surface, as seen in figure 3.1.

Thus, the topographic images do not exhibit molecular resolution due to the limited resolution of the microscope, as the tip used for the measurements has a radius of 10 nm, resulting in a lateral resolution of approximately 0.4 nm, which is very close to the dimensions of the molecule ($a = 0.9$ nm, $b = 0.4$ nm, and $c = 0.5$ nm) [50].

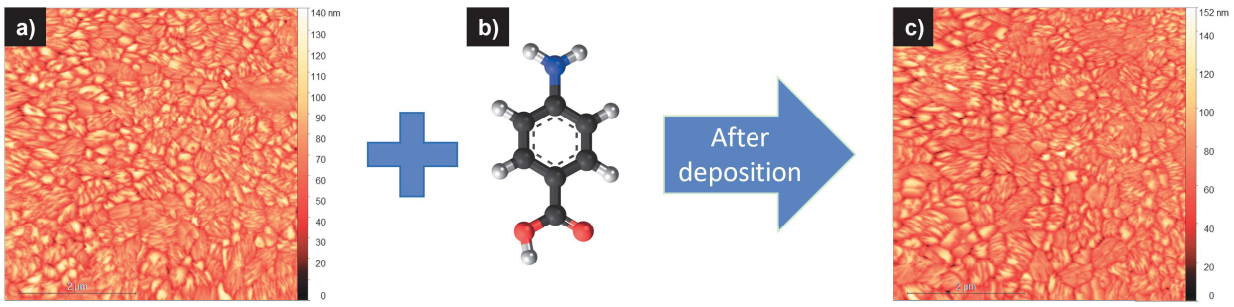

Figure 3.1: AFM topographic images of $5000 \times 5000\ nm^2$, a) bare 100 nm thicknesses V_2O_5, b) representative scheme of the molecule, and c) topographic image with molecules.

3.2 Identification of the SAMs formation by XPS and Density Functional Theory simulations

From the XPS spectrum with a broad energy range (1200 - 0 eV), we observe the same signals as before deposition, which are related to oxygen, vanadium, nitrogen, and carbon species. Therefore, the sample was eroded in UHV to remove the nitrogen contaminant, which was confirmed by in-situ XPS. Subsequently, the sample was taken out from the vacuum chamber to be functionalized with PABA. The equivalent homogeneous atomic fraction is summarized in table 3.1, where the increase in carbon and nitrogen atomic composition due to the presence of the molecule on the surface is observed. Furthermore, the initial carbon contamination was estimated from XPS measurements at normal emission by comparing the carbon-to-oxygen ratio of the signal intensities of the bare surface with the functionalized one, resulting in an approximate 30% contamination relative to the carbon intensity of the PABA molecules.

V_2O_5 surfaces	Vanadium	Oxygen	Carbon	Nitrogen
bare V_2O_5	22.8	60.2	16.0	1.0
Eroded V_2O_5	21.3	58.9	19.8	0.0
PABA V_2O_5	14.7	45.9	35.9	3.5

Table 3.1: Percentage of atomic concentration of bare V_2O_5, eroded V_2O_5 and PABA V_2O_5

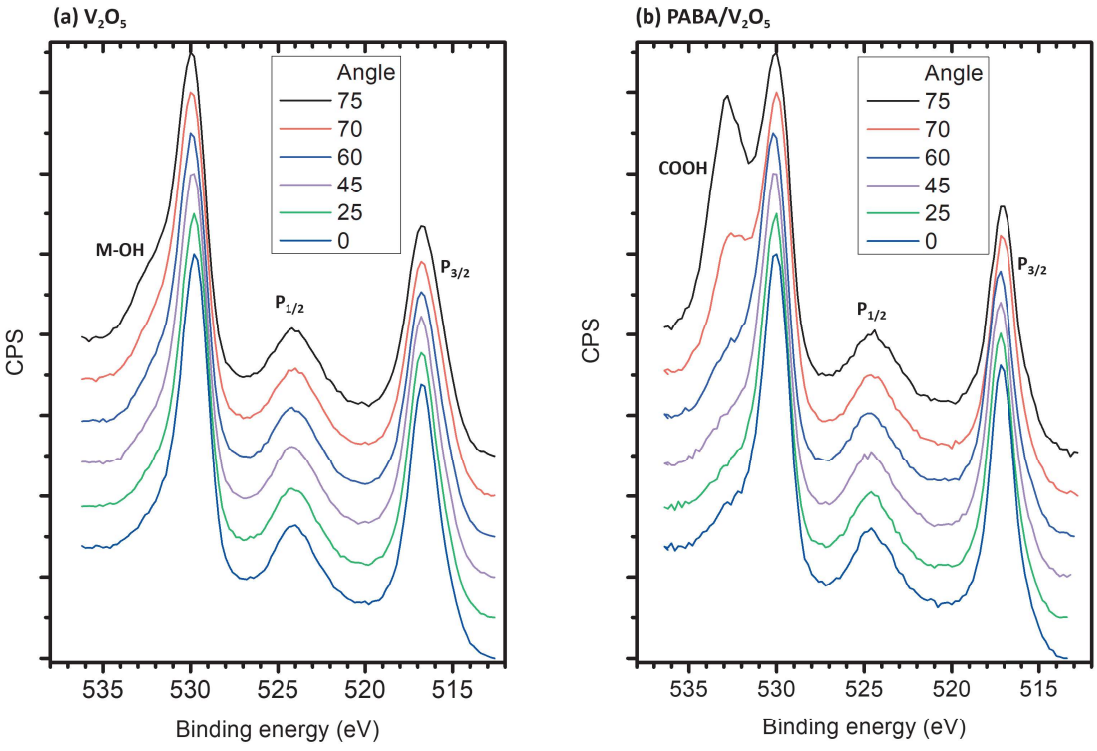

Figure 3.2: Angle resolved XPS of V-O spectra from a) bare V_2O_5 and b) PABA/V_2O_5

A deeper analysis by HR-XPS of bare V_2O_5 and $PABA/V_2O_5$ samples shows a higher pres-

ence of $-O^*H$ at 531.5 eV on the uppermost surface when functionalized, see figure 3.2. This is associated with the carboxylic functional group, confirming the presence of the molecule. Additionally, the nitrogen and carbon spectra allow us to distinguish the signals associated with benzene and the NH_2 functional group, as displayed and indicated in figure 3.3.

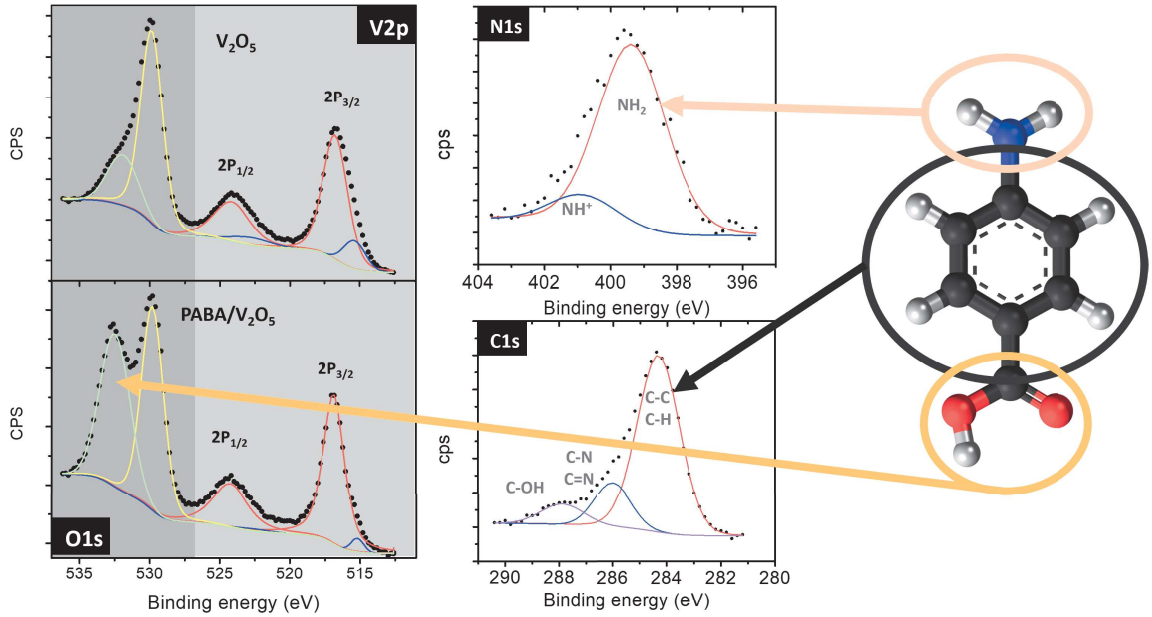

Figure 3.3: XPS of bare and PABA caped V_2O_5 and the molecule schematic. The O1s and V2p signals are displayed for V_2O_5 bare surface, and C1s, N1s, O1s and $V2p$ signals are displayed for PABA-SAMs/V_2O_5.

Additionally, the $V^{+5} : V^{+4}$ ratio observed on the bare V_2O_5 surface was near 15 : 1, as mentioned earlier. However, when functionalizing with PABA, the $V^{+5} : V^{+4}$ ratio increases to 25 : 1, indicating further oxidation of vanadium during functionalization. This increase suggests a low percentage of oxygen vacancies in the functionalized sample.

Density functional theory (DFT) simulations were conducted by Fabian Dietrich and Eduardo Cisternas at Universidad de La Frontera using Quantum Espresso. These simulations were based on the crystal structure of α-V_2O_5 with Pmmn symmetry, which was obtained from 'The Materials Project' web page [51]. To model the system effectively, a supercell of 1 x 3 x 3 unit cells was constructed. Additionally, a 20 Å vacuum space was added above the top layer in the [001] direction to create a slab. The supercell optimization was carried out with the bottom layer held fixed, as depicted in Figure 3.4 (left).

Next, a single molecule of PABA was placed on the optimized surface in different configurations: standing up and interacting through the carboxylic group (left) or through the amino group (right), as well as lying down and other twisted or displaced positions. The new systems with molecules on the surface were then re-optimized to calculate the adsorption energies and the differences in dispersion correction, determining the most stable configuration, shown in figure 3.4. Additionally, the same analysis was carried out for one, two, or three

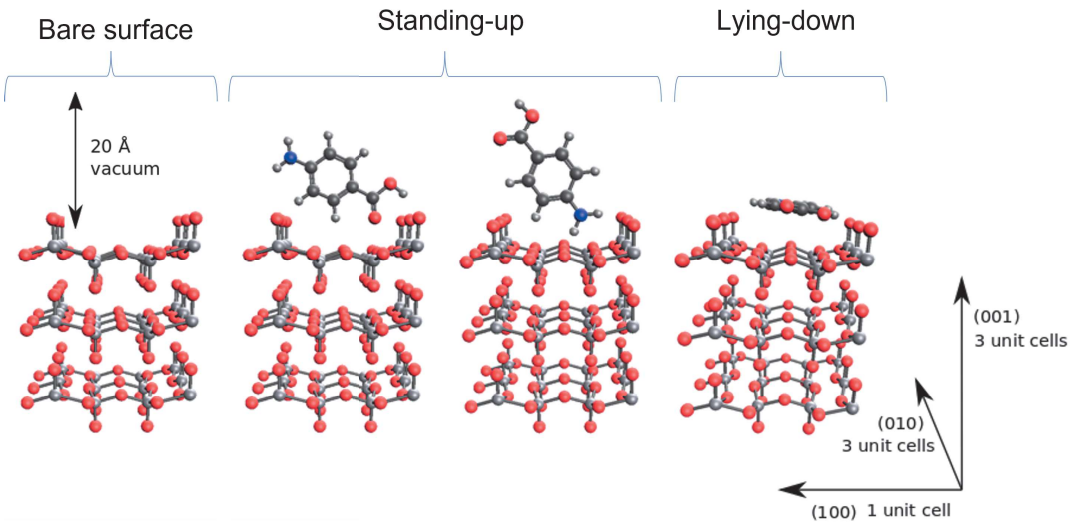

Figure 3.4: The vanadium pentoxide bare surface is depicted, accompanied by three potential adsorbed PABA molecule configurations. On the left, the vanadium pentoxide supercell spans 1x3x3 unit cells. In the center, PABA molecules are situated in a standing-up configuration: on the left, interacting through the carboxylic group (designated as configuration CO_1), and on the right, interacting through the amino group (referred to as configuration NH_1). Lastly, on the right, a configuration denoted as flat_1 portrays the molecule lying down on the surface.

molecules on the surface, calculating the adsorption energy per molecule and the interaction energy between the molecules.

The results showed that when there are few PABA molecules on the surface, the most stable configuration is lying-down. However, as the concentration of molecules increases, the standing up configuration with the carboxylic group interacting with the surface becomes more stable. The tables below display the adsorption and dispersion energies of the most probable configurations for one molecule on the surface (table 3.2), and for two and three molecules (table 3.3). Figure 3.5 provides a schematic representation of these configurations.

Configuration	$E_{\text{ads}}^{\text{D2}}$/eV	$\Delta E_{\text{disp}}^{\text{D2}}$/eV	$E_{\text{ads}}^{\text{D3}}$/eV	$\Delta E_{\text{disp}}^{\text{D3}}$/eV
CO_1	-1.37	-0.39	-0.98	-0.46
flat_1	-2.28	-0.88	-1.25	-0.95
flat_2	-2.13	-0.86	-1.35	-0.93
flat_3	-1.99	-0.90	-1.24	-0.96

Table 3.2: Adsorption and dispersion energies for different configurations of a PABA molecule adsorbed on the V_2O_5 surface, using D2 and D3 dispersion corrections.

Afterwards, the system was expanded to 20 layers of vanadium pentoxide to simulate the XPS spectrum of a slab of more than 10 nm thickness, considering an exponential decay of the intensity, as shown in equation 3.1.

$$I(z) \sim \sigma(h\nu, \theta) exp\left(\frac{-z}{\lambda cos(\theta)}\right) \tag{3.1}$$

Configuration	$E^{D2}_{\text{ads, ag.}}$	$E^{D2}_{\text{ads,m}}$	E^{D2}_{int}	$\Delta E^{D2}_{\text{disp}}$	$E^{D3}_{\text{ads, ag.}}$	$E^{D3}_{\text{ads,m}}$	E^{D3}_{int}	$\Delta E^{D3}_{\text{disp}}$
CO+CO_1	-3.14	-1.57	-0.42	-1.19	-1.95	-0.97	+0.01	-1.25
CO+CO_2	-3.13	-1.57	-0.42	-1.20	-1.97	-0.98	-0.01	-1.26
CO+CO+CO_1	-5.38	-1.79	-1.33	-2.23	-2.97	-0.99	-0.04	-2.33
CO+CO+CO_2	-5.38	-1.79	-1.33	-2.17	-3.06	-1.02	-0.13	-2.29
flat+flat+flat_1	-3.80	-1.27	-	-1.99	-2.00	-0.67	-	-1.94

Table 3.3: Adsorption, interaction and dispersion energies for different configurations of two and three PABA molecules adsorbed on the V_2O_5 surface, all values in eV.

where z is the depth of the atom, λ is the inelastic mean free path (IMFP) of the photoelectrons in V_2O_5 (21.78 Å) [52, 53] and θ is the angle of the detected electrons relative to the surface, and σ is the elastic-scattering cross section. The elastic-scattering cross section was obtained from NIST Database [54] at an energy $h\nu = 1487$ eV. Therefore, those theoretical XPS calculations were made with the most probable standing-up and lying-down configurations.

Afterward, the experimental data of carbon and nitrogen species show a ratio $C : N$ between 8 and 11 (figure 3.6a), while the theoretical calculations indicate values between 5.4 and 6.4 for the standing-up configuration and 6.8 for the lying-down configuration, implying a higher concentration of carbon, which is associated with contaminants from the adventitious carbon [55]. This carbon contamination was estimated at 30% as mentioned above, so this value was included in the simulation, obtaining values of C/N between 8 and 10, fitting the experimental data better. Observing the C/O and C/V ratios (figure 3.6b), the uncontaminated simulation of the standing-up configuration (brown line) fits the experimental data well, while considering the contamination, the curve (in red) shows slightly higher values than the experiment. For the N/O and N/V ratios (figure 3.6c and f), the up-standing configuration provides higher values than the experiment, and the lying down provides lower values. Consequently, we assume that the surface is not homogeneously covered by up-standing molecules but that there are also areas with lying-down molecules.

Given the experimental results, we expect the configuration of the molecules to be up-standing with zones in a lying-down orientation, which is consistent with the theoretical results. This is in agreement with the proposed configuration of chemisorbed PABA on TiO_2 [56] and $Li_{1.2}Ni_{0.6}Mn_{0.2}O_2$ [38].

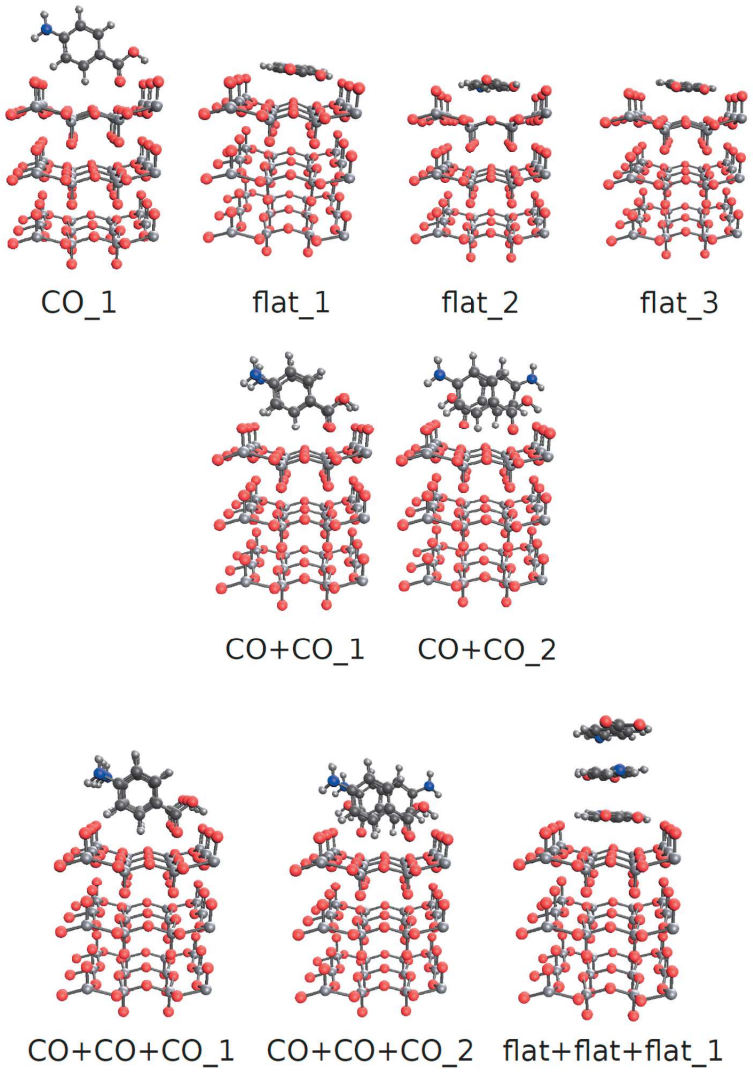

Figure 3.5: Schematic representation of different configurations of PABA SAM adsorbed onto vanadium pentoxide, including standing-up and lying-down orientations with one molecule (top), two molecules (middle), and three molecules (bottom).

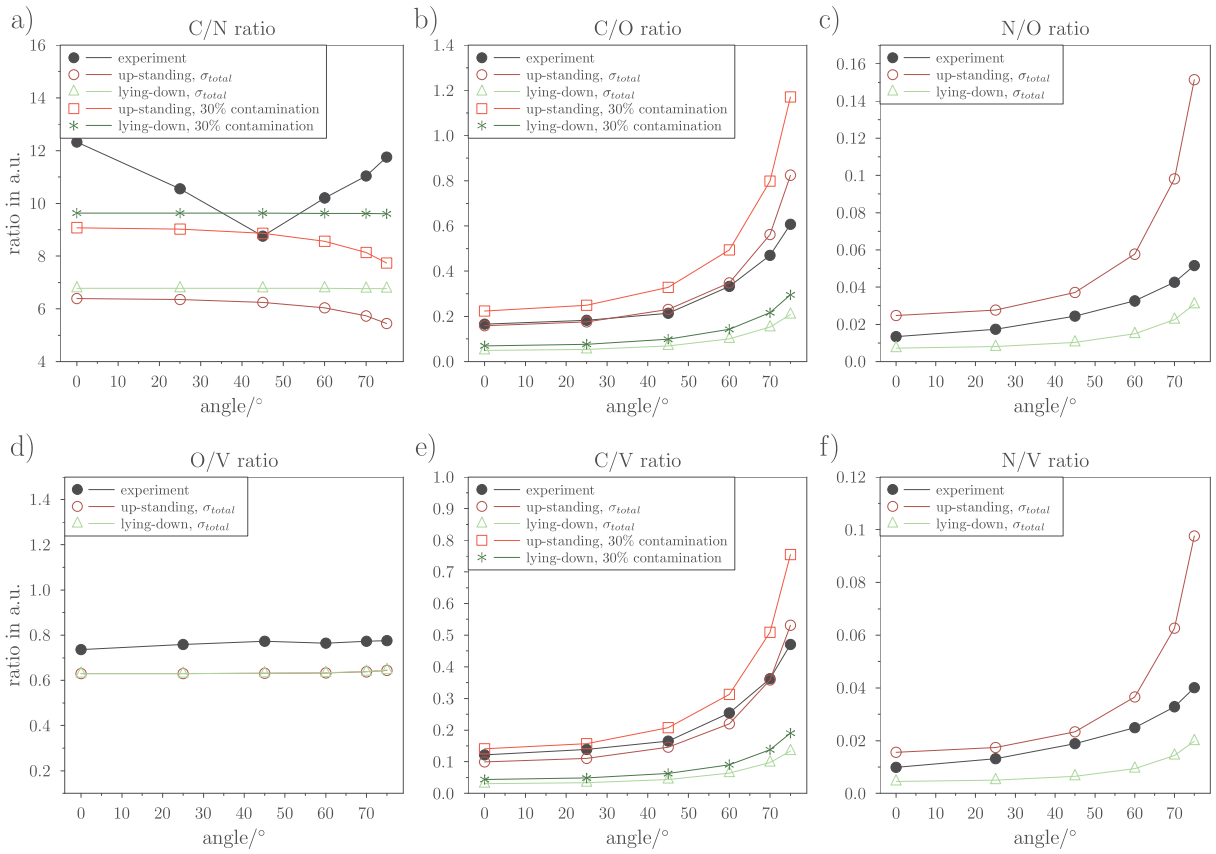

Figure 3.6: Angular study of the ratio of atomic species detected on the PABA-SAMs/V_2O_5 surfaces

Chapter 4

Study of para-(phenylazo)benzoic acid onto vanadium pentoxide surface

The study of PABA self-assembled monolayers formation onto vanadium pentoxide shows that PABA molecules get adsorbed through the carboxylic functional group. Therefore, to enhance the performance of vanadium pentoxide as a cathode for batteries, one can consider choosing a molecule that has the carboxylic functional group, which has the potential to be adsorbed onto the surface, along with another less reactive functional group that would not block lithium intercalation. Furthermore, in this chapter, we investigate vanadium pentoxide surfaces with a thickness of 150 nm, fabricated onto stainless steel, their functionalization with para-(phenylazo)benzoic acid (PPBA), and their effects on the performance as cathode materials for lithium-ion batteries.

4.1 Surface characterization

Vanadium pentoxide surfaces were deposited by the method described in Chapter 1 onto stainless steel, resulting in a 50 nm thick layer of metallic vanadium, which upon oxidation reached a thickness of 150 $\pm$ 5 nm. Subsequently, AFM topographic images were taken, revealing a roughness RMS of 18 nm, lower than that observed in samples onto silicon (RMS = 32 nm). Additionally, it was observed that this roughness value remained unchanged when functionalizing with PPBA, as the size of the molecule is still smaller than the resolution limit of the microscope, similar to the PABA molecule. Furthermore, conductive AFM was performed to study the electrical properties of both surfaces: bare and PPBA-capped V_2O_5. Differences in conduction between steps and terraces of the structures were observed, as shown in figure 4.1, where lighter sites in the current image (right panel) indicate higher conduction. Figure 4.2 provides a more detailed view of steps and terraces, where (a) displays the AFM topographic image, (b) shows the IV curves for steps and terraces, and (c) displays the lines profile of two terraces connected by one step.

Furthermore, IV curves were obtained to observe the conduction behavior from -2 V to 2 V, as shown in figure 4.2(c). In this voltage range, the terraces (continuous line) exhibit

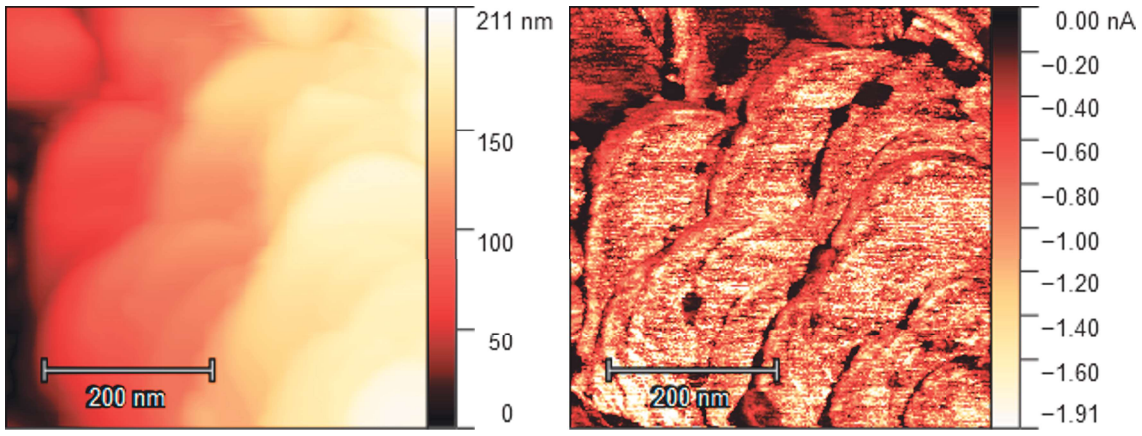

Figure 4.1: AFM topographic and C-AFM current images of the same spot on the bare V_2O_5 surface. The current image was taken at -1 V. Both are images of 500×500 nm^2

higher conduction than the steps (segmented line), and this trend was consistent on both the bare V_2O_5 surface (red lines) and the PPBA-capped surface (blue lines). Moreover, functionalizing with PPBA increased the difference in conduction, favoring the conduction of electrons through terraces over steps.

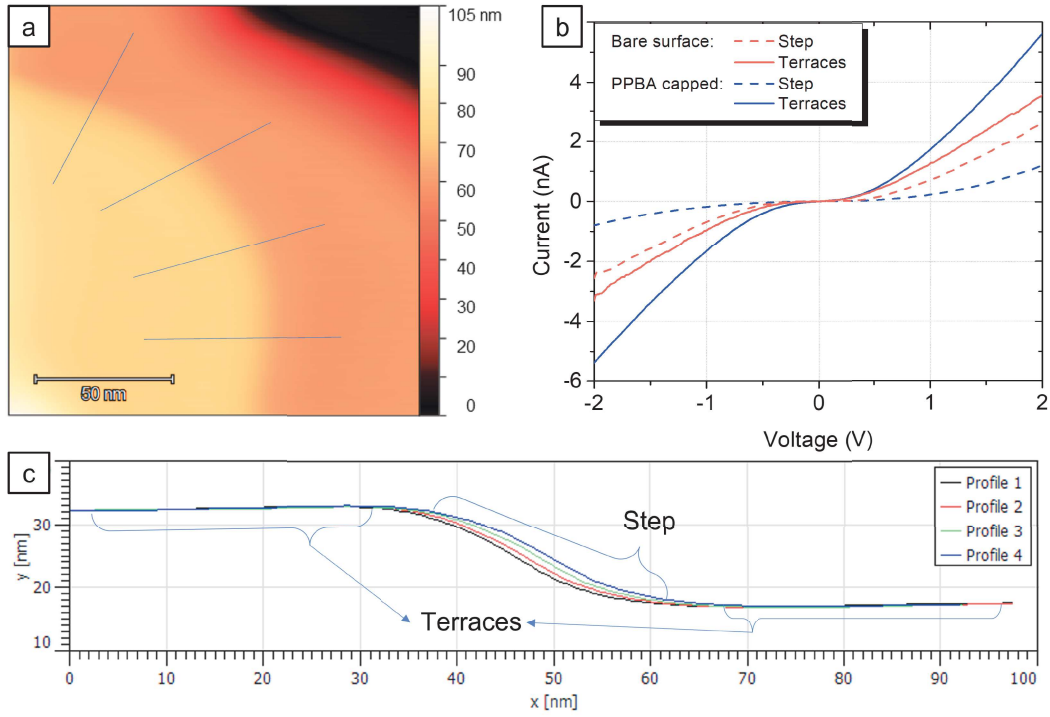

Figure 4.2: Conductive AFM, a) topographic image of the terraces and the step, b) IV curves of both terraces and steps and c) Line profiles of two terraces connected by means of one step

4.2 Chemical characterization

From the XPS spectrum with a broad energy range (1200 eV - 0 eV) of both bare and PPBA-capped V_2O_5, it is observed that the signals are related to oxygen, vanadium, nitrogen, and carbon species. Furthermore, the presence of iron (Fe) close to 1% of the signal aligns with the coverage results found on Si. In the bare sample, the signals of carbon and nitrogen are related to adventitious carbon and adsorbed nitrogen, consistent with the results from the samples on Si. Thus, when functionalizing with PPBA, the proportion of nitrogen and carbon increases as the oxygen and vanadium decrease, due to the presence of the molecule on the surface. See figure 4.3 and table 4.1.

V_2O_5 surfaces at 25°	Vanadium	Oxygen	Carbon	Nitrogen
bare V_2O_5	16.7	58.7	23.4	1.2
PPBA V_2O_5	15.5	53.9	28.3	2.3

Table 4.1: Percentage of atomic concentration of bare V_2O_5, and PPBA V_2O_5

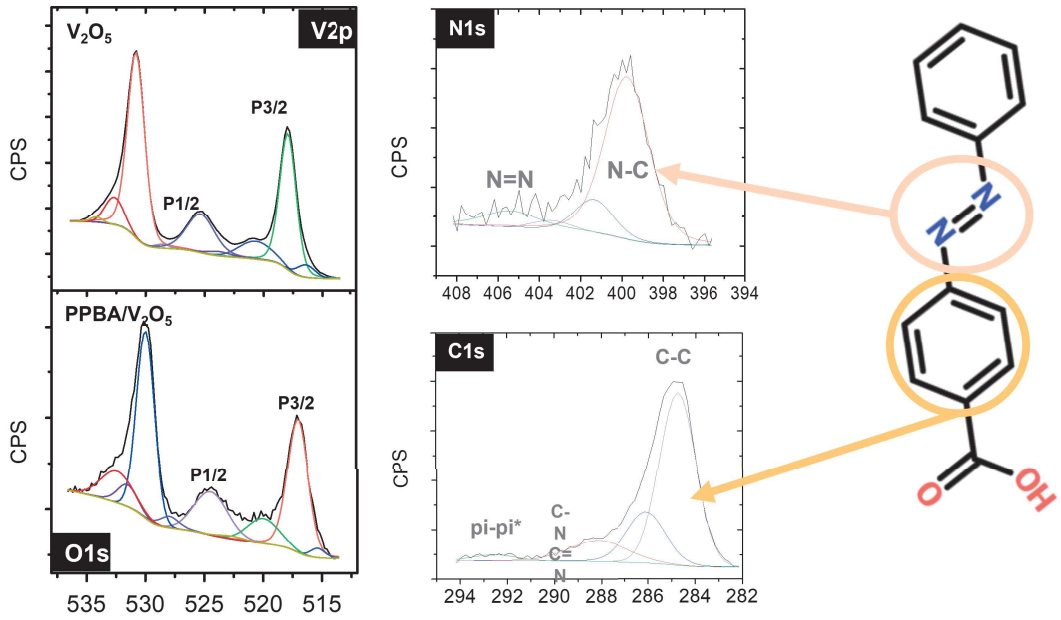

Figure 4.3: XPS for bare and PPBA capped V_2O_5 and the molecule schematic. The V2p and O1s spectrum is displayed for V_2O_5 bare surface, and C1s, N1s, O1s and V2p spectra are displayed for PPBA capped V_2O_5

Through a detailed analysis of those quantities, the amount of oxygen bonded to vanadium in the bare surface can be separated from the oxygen in contaminants and related to carbon in contaminants, where a carbon-to-oxygen ratio of $C : O \sim 1.4 : 1$ is found, as summarized in table 4.2. Then, the V_2O_5 oxygen is separated from those of the molecule and contamination in PPBA-capped V_2O_5. Also, as the molecule has the chemical composition $C_{13}H_{10}N_2O_2$, a ratio $C : O : N \sim 13 : 2 : 2$ is expected since hydrogen cannot be measured by XPS.

Therefore, by maintaining the contamination ratio found in the bare surface considering and the PPBA chemical composition, it is found that 10% of the oxygen, 33% of the carbon and 57% of the nitrogen excess in the PPBA-capped surface are from the PPBA molecule, and the rest is from contamination and adsorbed nitrogen. The summary is shown in table 4.2.

	Vanadium	**Oxygen**	**Carbon**	**Nitrogen**
Bare V_2O_5	16.7	58.7	23.4	1.2
V_2O_5	16.7	41.8	$\sim$	$\sim$
N_{ads}	$\sim$	$\sim$	$\sim$	1.2
Contaminants	$\sim$	16.9	23.4	$\sim$
PPBA-V_2O_5	15.5	53.9	28.3	2.3
V_2O_5	15.5	38.7	$\sim$	$\sim$
PPBA	$\sim$	1.5	9.4	1.3
Contaminants	$\sim$	13.7	18.9	$\sim$
N_{ads}	$\sim$	$\sim$	$\sim$	1.0

Table 4.2: Atomic concentration breakdown of bare V2O5 and PPBA V2O5, where in bare V2O5 it is distinguishing pure V2O5, adsorbed nitrogen, and contaminants, and in PPBA V2O5, it is distinguishing pure V2O5, adsorbed nitrogen, PPBA (expected) and contaminants concentrations.

The HR-XPS spectra of vanadium and oxygen show a major proportion of V^{+5} than V^{+4} in both samples, bare and PPBA-capped V_2O_5. Thus, when observing the AR-XPS of the bare sample, an increase in vanadium V^{+4} at larger angles is observed, indicating a thin VO_2 over-layer in the upmost surface, as shown in figure 4.4(a). On the other hand, when observing the PPBA-V_2O_5 surface, the V^{+4} concentration first increases with the angle, and then it decreases at the upmost surface, as seen in figure 4.4(b), indicating that the molecule further oxidizes the upmost surface when functionalizing, reducing the thin VO_2 over-layer. Additionally, the angle-resolved XPS for the carbon signal shows an increase in the $C-C : C-OH$ ratio at higher measurement angles (see figure 4.4(c)), meaning that the $C-C$ peak is more superficial than $C-OH$, indicating that the molecules interact with the surface through the carboxylic group rather than the benzene ring. Furthermore, the $C-C$ peak was found at 284.8 eV, thus, the benzene rings are not interacting with the surface.

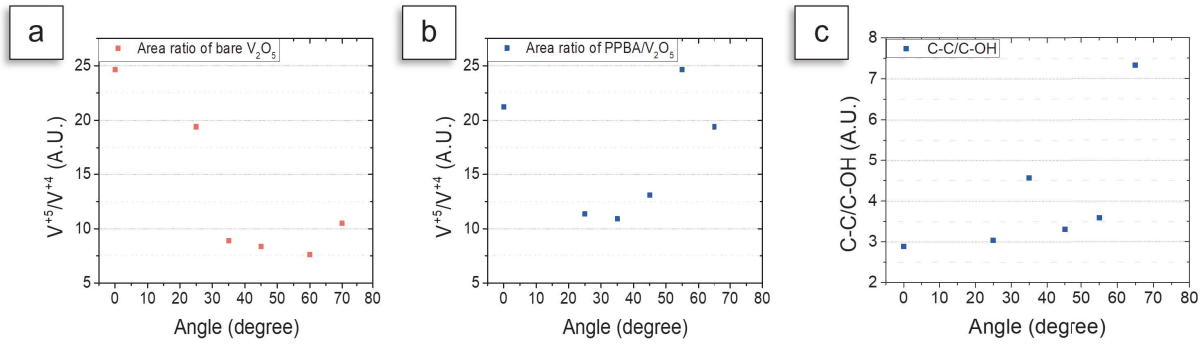

Figure 4.4: Vanadium oxide state ratio (V^{+5}/V^{+4}) from angle resolved XPS for a) bare V_2O_5, b) PPBA capped V_2O_5 and c) angle resolved carbon C-C/C-OH ratio

Afterwards, the thickness of the VO_2 over-layer and other species are estimated from the

equation 4.1 derived by Strohmeier [57], where the subscript x indicates the species to study, d is the thickness of the over-layer, λ is the inelastic mean free path of the photoelectrons, θ is the angle of measurement with respect to the plane of the sample, N is the atomic density, and σ is the ionization cross-section of the photoelectrons. The cross-section parameters were obtained from the NIST database[54], and the inelastic mean free path and mass densities from QUASES software [52].

$$\mathrm{d}_x = \lambda_x sin(\theta_{takeoff}) \left(1 + \frac{N_{V_2O_5}}{Nx} \frac{I_x/\lambda_x\sigma_x}{I_v/\lambda_v\sigma_v + I_o/\lambda_o\sigma_o}\right) \tag{4.1}$$

Therefore, by replacing the variables with the intensities obtained from the HR-XPS spectra and the measurement angles, the over-layer of VO_2 in the surfaces was calculated, which is 4.1% of ML in the bare surface, and 2.8% of ML in the PPBA-capped surface, confirming the further oxidation of the over-layer. Moreover, the decrease in adsorbed nitrogen when functionalizing with PPBA is consistent with the decrease in VO_2, since the atmospheric nitrogen is mainly adsorbed onto V^{+4} sites [46]. Additionally, the adventitious carbon layer was estimated at 13.2% of ML for the bare surface and 11.0% for the PPBA-capped.

On the other hand, the nitrogen layer was estimated at 4.5% ML onto the bare surface and 8.3% ML for the PPBA-capped surface. Since the nitrogen in the molecule is 57% of the total amount, there are 4.8% ML of nitrogen from the molecule. Therefore, using the atomic density and the thickness of the nitrogen layer, we can express the nitrogen layer in terms of the number of nitrogen molecules (two atoms) per square centimeter, that is, 4.8% ML $\sim 3.5 \times 10^{13}$ molec/cm^2. Furthermore, since each PPBA molecule has two nitrogen atoms, the calculated density of nitrogen molecules is the same as PPBA molecules on the surface, which is very similar to the coverage obtained by Nicolau et al. [37]. Additionally, by multiplying this density by the area of the V_2O_5 unit cell (A = a·b = 0.41 nm^2), we obtain the amount of molecules on the surface, which is equivalent to 0.14 molecules for every two V_2O_5 formula units.

4.3 Surface density of states and electrochemical analysis

From DFT simulations using Quantum Espresso with the same configuration described in Chapter 3, the density of states for the bare surface was calculated, as shown in figure 4.5(a). An energy gap close to 2 eV is observed, slightly lower than that of the bulk (2.28 eV), as seen in figure 4.5(b). Therefore, the DFT calculation of the surface with PPBA was made with a configuration similar to that with the PABA molecule. The structure used to calculate the DOS is shown in figure 4.5(c), and their respective density of states is shown in figure 4.5(d). In this last structure with PPBA, the Fermi energy moves close to 1 eV at higher energies compared to the bare surface, and electronic states of the molecule from carbon, nitrogen, and oxygen appear within the gap. Consequently, the highest occupied molecular orbital (HOMO) of the surface changes from V_2O_5 atoms to nitrogen and carbons of the molecule, as shown in figure 4.5(d).

Furthermore, the samples were assembled as cathodes for lithium batteries and were subjected to cyclic voltammetry and cyclability measurements in both ranges $2.6 - 4$ V and $2 - 4$ V. Additionally, from cyclic voltammetry in the range $2.6 - 4$ V, the phase transitions associated with $\alpha V_2O_5 \leftrightarrow \varepsilon V_2O_5$ and $\varepsilon V_2O_5 \leftrightarrow \delta V_2O_5$ were observed at 3.41 V and 3.24 V,

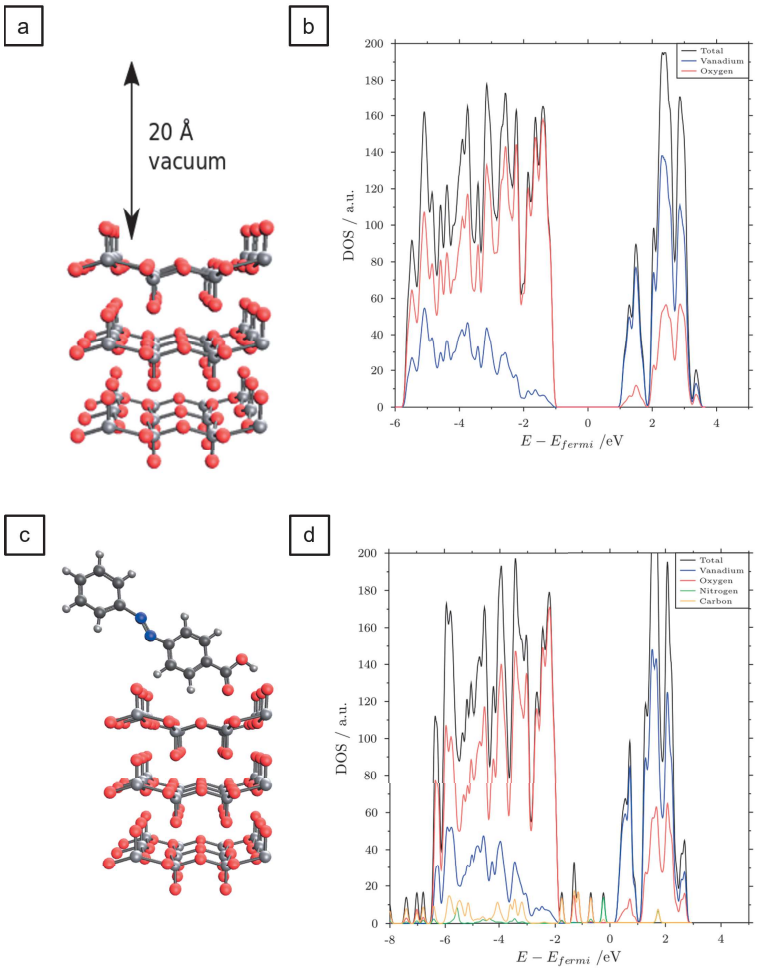

Figure 4.5: a) Structure and b) Density of States for the bare vanadium pentoxide surface. c) Structure and d) Density of States for the vanadium pentoxide surface functionalized with the PPBA molecule.

respectively, as seen in figure 4.6(a). Additionally, in the $2-4$ V range, peaks associated with the $\delta V_2O_5 \leftrightarrow \gamma V_2O_5$ phase transition were observed at 2.38 V. The phase transitions found are consistent with the theoretical results reported in [35] (refer to Figure 3). Moreover, the peak associated with $\varepsilon V_2O_5 \leftrightarrow \delta V_2O_5$ showed a shift of 0.02 V at higher voltages, due to a shift of 0.04 V in their oxidation curve, as shown in figure 4.7(a). Due to this increase in the peak-to-peak distance, the $\varepsilon V_2O_5 \leftrightarrow \delta V_2O_5$ phase transition is less electrochemically reversible when cycling in the $2-4$ V range. The phase transition potential and the difference between oxidation and reduction peaks are summarized in tables 4.3 and 4.4, respectively.

On the other hand, cyclability measurements were made in both ranges, 2.6-4 V and 2-4 V. The charge and discharge capacity per mass unit was calculated by using a mass of 6.3×10^{-5} g. This calculation is based on the density of bulk vanadium pentoxide obtained from the Materials Project [58] and involves multiplying by the thickness (150 nm) and the area of the coin cells (123 mm^2), which remains consistent across all surfaces. From the samples cycled in the 2.6-4 V range, it is observed that the PPBA-capped V_2O_5 has both charge and discharge capacity near 80 mAh/g, lower than the bare V_2O_5 with a charge capacity

Surface	Voltage range [V]	$E_{1/2}$ $\alpha \leftrightarrow \varepsilon$ [V]	$E_{1/2}$ $\varepsilon \leftrightarrow \delta$ [V]	$E_{1/2}$ $\delta \leftrightarrow \gamma$ [V]
Bare	2,6-4	3,41	3,24	$\sim$
PPBA	2,6-4	3,41	3,24	$\sim$
Bare	2-4	3,41	3,26	2,38
PPBA	2-4	3,41	3,26	2,38

Table 4.3: $E_{1/2}$ potential obtained in different phase transitions for Bare and PPBA V_2O_5 in $2,6-4$ and $2-4$ V voltage ranges

Surface	Voltage range [V]	ΔE $\alpha \leftrightarrow \varepsilon$ [V]	ΔE $\varepsilon \leftrightarrow \delta$ [V]	ΔE $\delta \leftrightarrow \gamma$ [V]
Bare	2,6-4	0,03	0,10	$\sim$
PPBA	2,6-4	0,03	0,10	$\sim$
Bare	2-4	0,03	0,14	0,16
PPBA	2-4	0,03	0,14	0,17

Table 4.4: Difference in oxidation and reduction potential for each phase transition for Bare and PPBA V_2O_5 in the $2,6-4$ and $2-4$ V voltage range

near 100 mAh/g and discharge capacity near 90 mAh/g, as shown in figure 4.6(b). However PPBA-V_2O_5 presents a higher surface stability since a higher energy efficiency is observed from the first cycles, as shown in figure 4.6(c).

Furthermore, when cycling in the voltage range $2-4$ V, the energy efficiency of PPBA-capped V_2O_5 is still higher than bare V_2O_5, and the efficiency of both increases compared to cycling in the $2.6-4$ V range, as shown in figure 4.7(c). Moreover, the charge and discharge capacity of the PPBA-V_2O_5 starts at 175 mAh/g and is initially higher than the bare surface. However, it gradually decreases over the first 60 cycles until it becomes equal to the charge/discharge capacity of bare V_2O_5 which is 150 mAh/g, as shown in figure 4.7(b). These results, together with the increase in conductivity shown in figure 4.2(c), may indicate a higher ionic conductivity of V_2O_5 due to the functionalization with PPBA.

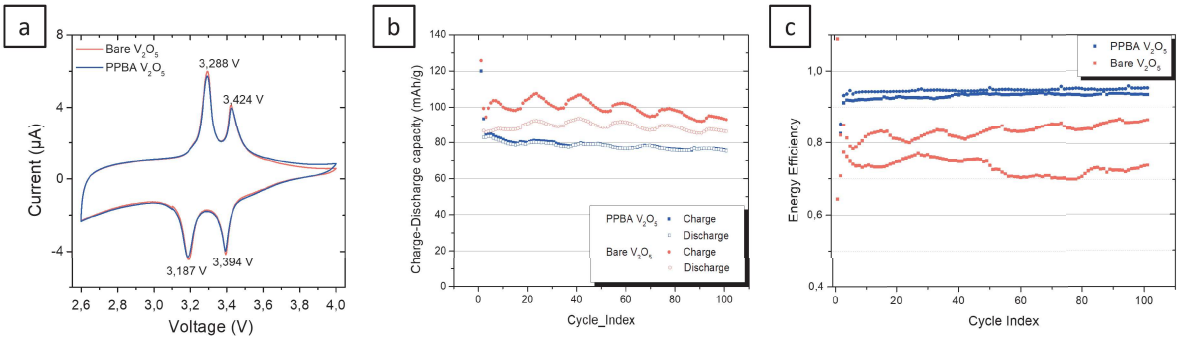

Figure 4.6: a) Cyclic voltametry, b) Cyclability and c) energy efficiency of bare and PPBA capped surfaces in 2.6-4 V range

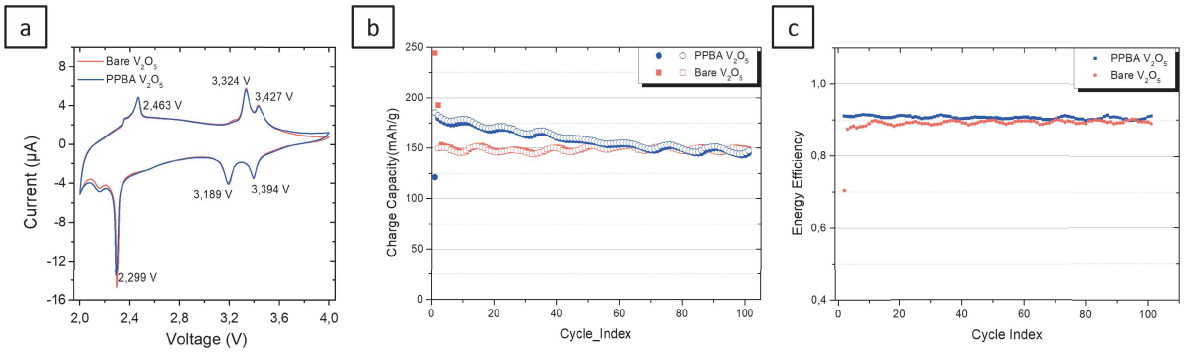

Figure 4.7: a) Cyclic voltametry, b) Cyclability and c) energy efficiency of bare and PPBA capped surfaces in 2-4 V range

4.4 Post mortem analysis

Postmortem analysis was performed using XPS at two angles: 0° (normal emission) and 70° (grazing angle). In the lithium spectra from normal emission, the presence of metallic lithium (Li^0) at 54.7 eV is observed, probably due to lithium atoms trapped within the lattice, along with signals from lithium hydroxide (LiOH) or lithium carbonate (Li_2CO_3) at 55.4 eV, resulting from the degradation of the electrolyte. An additional signal at 56.3 eV is observed in one sample of bare V_2O_5, corresponding to lithium fluoride (LiF). When observing the grazing angle spectra, the presence of Li_2CO_3 or LiOH, as well as Li^0 is observed, see figure 4.8.

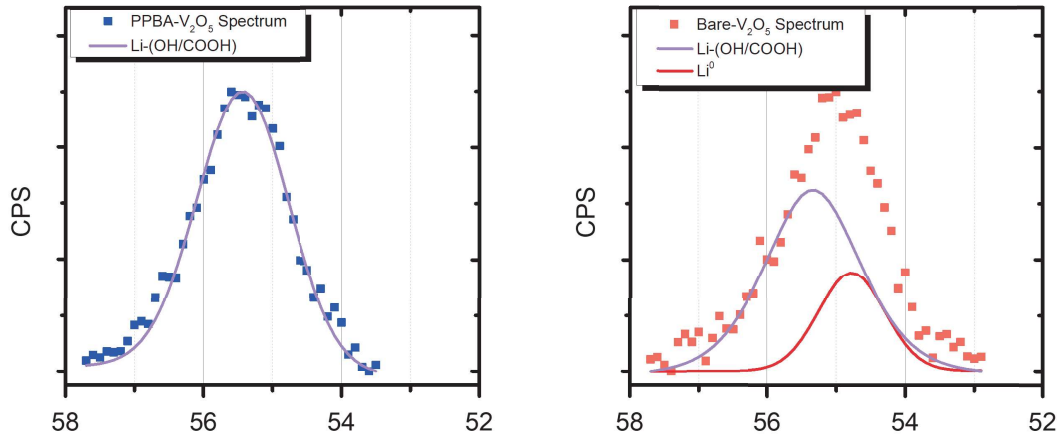

Figure 4.8: Lithium spectra for a) PPBA capped V_2O_5 and b) Bare V_2O_5

Furthermore, on the PPBA-V_2O_5 surface, no metallic lithium is detected. In the oxygen spectra, signals associated with lithium bonds in Li_2CO_3 or LiOH are observed at 532.2 eV binding energy, along with an additional signal for the oxygen double bond $-C = O*$ in Li_2CO_3 at 533.2 eV. Additionally, in both the lithium and oxygen spectra, a higher concentration of LiOH and Li_2CO_3 is observed in the PPBA-capped V_2O_5, as shown in figure 4.9.

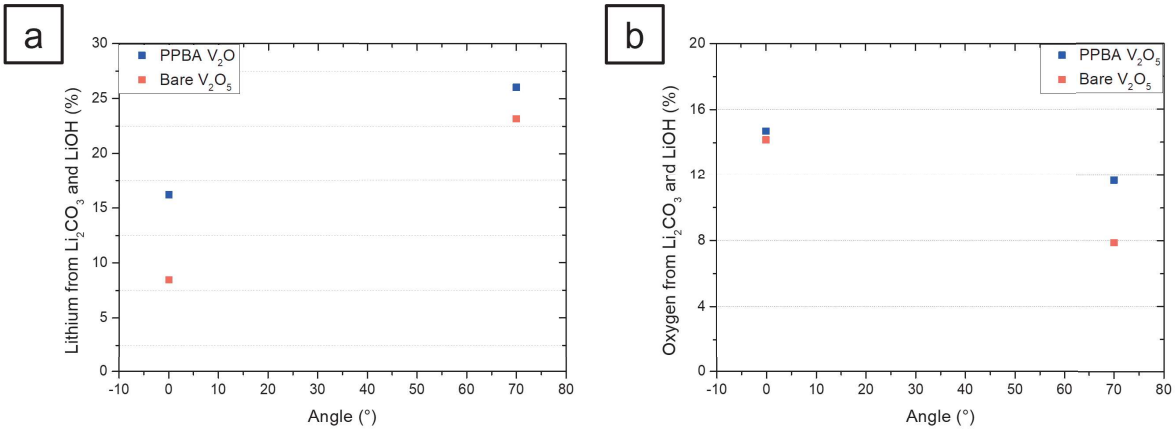

Figure 4.9: Atomic concentration of Lithium and oxygen from Li_2CO_3 and LiOH

Moreover, the phosphorus spectra show signals related to the presence of lithium salts, either from $LiPF_6$ in the electrolyte or from its degradation in the form of Li_zPF_x, both at $P2p_{3/2} = 136.7$ eV binding energy, along with oxidized lithium salts of the form $Li_zPF_xO_y$ at $P2p_{3/2} = 133.2$ eV. Additionally, a signal related to P_2O_5 is found in those spectra at $P2p_{3/2} = 134.8$ eV.

In the fluorine spectra, signals related to F^- anions and lithium salts (Li_zPF_x) are found at 684.8 and 686.9 eV, respectively. A signal at 688.4 eV is also observed, which is attributed to C-F bonds [59, 60]. Furthermore, in the PPBA-V_2O_5 spectra, a signal at 690.2 eV is found, which can be related to $LiPF_6$[61] or $Li_zPF_xO_y$[59] chemicals. Moreover, due to the absence of the LiF signal from the lithium spectra, the signal found at 684.8 eV from F anions must be from HF rather than LiF. By comparing these signals with that of Li_zPF_x, it is observed that the PPBA-V_2O_5 has a much lower concentration of degraded lithium salts compared to bare V_2O_5 (see figure 4.10).

Furthermore, in the vanadium spectra, an increase in V^{+5} concentration is observed at the upmost surface in the bare sample, while in PPBA-V_2O_5, a nearly constant value is observed. This difference can be attributed to a lower dissolution of the cathode, improving the stability in the PPBA capped surface (see figure 4.11).

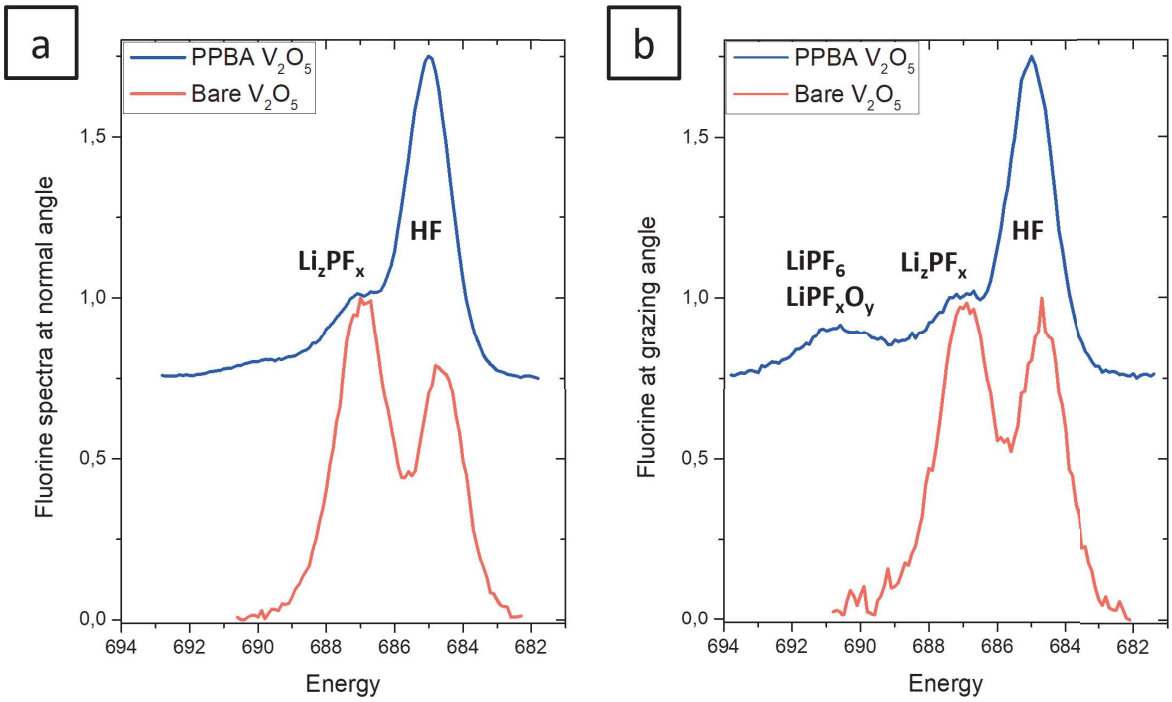

Figure 4.10: Post-mortem Fluorine spectra for bare and PPBA capped V_2O_5 a) at normal emission and b) grazing angle

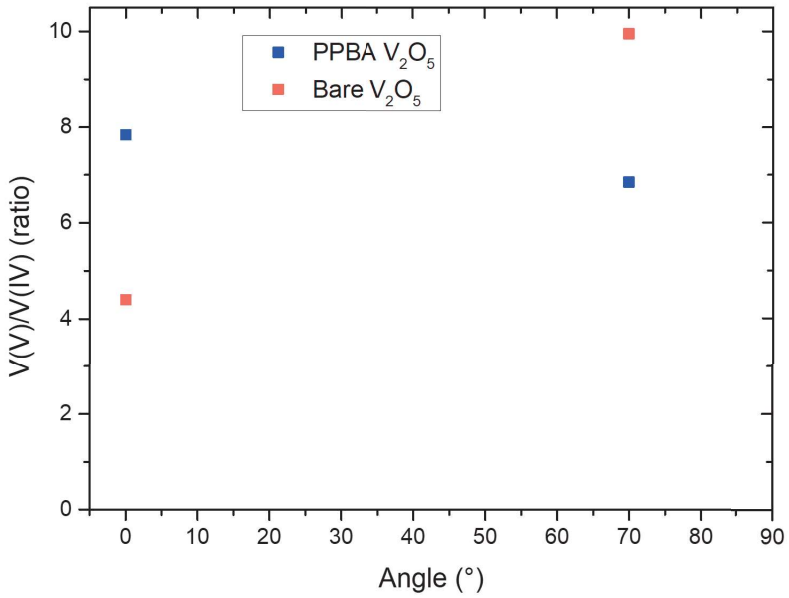

Figure 4.11: Vanadium oxide state ratio V^{+5}/V^{+4}

Chapter 5

Conclusions

Based on the preparation of vanadium pentoxide, after a meticulous characterization, the laminar arrangement of the films is evidenced. Therefore fabrication of vanadium pentoxide through the evaporation of metallic vanadium onto Si and subsequent oxidation in an oxygen atmosphere allows the fabrication of at least two different structures: nanobelts and disk-shaped structures by varying the thickness of deposited metallic vanadium. Furthermore, between 10 and 25 nm of evaporated metallic vanadium, there must be either a critical thickness where the structures change from nanobelts to disk-shaped, a range of thicknesses where both structures coexist, or a different structure type in between. The oxygen flow, treatment time, and temperature remain constant for all thicknesses; thus, the change in oxidation state at lower thicknesses is attributed to the change in structures observed through SEM and AFM. Additionally, vanadium pentoxide was successfully elaborated using the same method on stainless steel substrates, resulting in lower roughness.

Functionalization of vanadium pentoxide surfaces with molecules is possible on both silicon and stainless steel substrates through the carboxyl functional group, which further oxidizes the vanadium while maintaining surface roughness. This indicates the possibility of modulating the surface oxide state by functionalizing with molecules. Moreover, the concentration of carbon and oxygen contaminants decreases, likely due to displacement by the molecules, leading to a decrease in adsorbed nitrogen as well, owing to the reduction in V^{+4} active sites. Therefore, using the nitrogen concentration from the molecule, the density of molecules at the PPBA-capped surface was estimated and found to be at 1.4×10^{-1} molecules per V_2O_5 unit cell .

Furthermore, due to the absence of the carbon signal at $284,0$ eV and the preferred standing-up configuration at a high concentration of molecules, there are likely areas with several molecules in an upstanding configuration and areas with a low quantity of molecules lying down, or even without molecules. Additionally, DFT calculations show that the PPBA-capped surfaces exhibit states within the band-gap arising from carbon, oxygen, and nitrogen atoms in the molecules, which may be related to the increase in electronic conduction on the terraces. Moreover, there is a decrease in conduction within the steps

For the samples on stainless steel, the conduction within the terraces of the structures

is higher than that within the steps, and this difference is further magnified in the samples capped with PPBA. This increased contrast in conduction favors the movement of charge through the terraces rather than along the borders. It is likely that this phenomenon contributes to the improved charge/discharge capacity, resulting from enhanced electronic conduction aligned with the preferred lithium ion transport direction.

The formation of the PPBA SAM on the cathodic surface has a passivating effect on the same surface, protecting it from the corrosive action of hydrogen fluoride in the electrolyte

By introducing a protective SAM on a cathode surface, it is possible to alter the electronic states on the surface, resulting in a different electrochemical behavior.

Bibliography

[1] Kevin E Trenberth and John T Fasullo. Global warming due to increasing absorbed solar radiation. *Geophysical Research Letters*, 36(7), 2009.

[2] Trevor M Letcher. Climate change: observed impacts on planet earth. 2021.

[3] Oficina de Cambio Climático. Inventario nacional de gases de efecto invernadero y otros contaminantes climáticos, serie 1990-2018. 2020.

[4] Reed T Doucette and Malcolm D McCulloch. Modeling the prospects of plug-in hybrid electric vehicles to reduce co2 emissions. *Applied Energy*, 88(7):2315–2323, 2011.

[5] Alexander Zerrahn, Wolf-Peter Schill, and Claudia Kemfert. On the economics of electrical storage for variable renewable energy sources. *European Economic Review*, 108:259–279, 2018.

[6] Ahmed Zayed AL Shaqsi, Kamaruzzama Sopian, and Amr Al-Hinai. Review of energy storage services, applications, limitations, and benefits. *Energy Reports*, 2020.

[7] Hussein Ibrahim, Adrian Ilinca, and Jean Perron. Energy storage systems—characteristics and comparisons. *Renewable and sustainable energy reviews*, 12(5):1221–1250, 2008.

[8] J-M Tarascon and Michel Armand. Issues and challenges facing rechargeable lithium batteries. In *Materials for sustainable energy: a collection of peer-reviewed research and review articles from Nature Publishing Group*, pages 171–179. World Scientific, 2011.

[9] Da Deng. Li-ion batteries: basics, progress, and challenges. *Energy Science & Engineering*, 3(5):385–418, 2015.

[10] Da Deng, Min Gyu Kim, Jim Yang Lee, and Jaephil Cho. Green energy storage materials: Nanostructured tio 2 and sn-based anodes for lithium-ion batteries. *Energy & Environmental Science*, 2(8):818–837, 2009.

[11] Nikita O Kapustin and Dmitry A Grushevenko. Long-term electric vehicles outlook and their potential impact on electric grid. *Energy Policy*, 137:111103, 2020.

[12] Manal AlShafi and Yusuf Bicer. Thermodynamic performance comparison of various energy storage systems from source-to-electricity for renewable energy resources. *Energy*,

219:119626, 2021.

[13] Jinhuan Yao, Yanwei Li, Robert C Massé, Evan Uchaker, and Guozhong Cao. Revitalized interest in vanadium pentoxide as cathode material for lithium-ion batteries and beyond. *Energy Storage Materials*, 11:205–259, 2018.

[14] Meng Gu, Yang He, Jianming Zheng, and Chongmin Wang. Nanoscale silicon as anode for li-ion batteries: The fundamentals, promises, and challenges. *Nano Energy*, 17:366–383, 2015.

[15] Luning Wang, Anjali Menakath, Fudong Han, Yi Wang, Peter Y Zavalij, Karen J Gaskell, Oleg Borodin, Dinu Iuga, Steven P Brown, Chunsheng Wang, et al. Identifying the components of the solid–electrolyte interphase in li-ion batteries. *Nature chemistry*, 11(9):789–796, 2019.

[16] Kang Xu. Electrolytes and interphases in li-ion batteries and beyond. *Chemical reviews*, 114(23):11503–11618, 2014.

[17] Jordi Cabana, Bob Jin Kwon, and Linhua Hu. Mechanisms of degradation and strategies for the stabilization of cathode–electrolyte interfaces in li-ion batteries. *Accounts of chemical research*, 51(2):299–308, 2018.

[18] Weishan Li. An unpredictable hazard in lithium-ion batteries from transition metal ions: dissolution from cathodes, deposition on anodes and elimination strategies. *Journal of The Electrochemical Society*, 167(9):090514, 2020.

[19] Aurélie Guéguen, Daniel Streich, Minglong He, Manuel Mendez, Frederick F Chesneau, Petr Novák, and Erik J Berg. Decomposition of lipf6 in high energy lithium-ion batteries studied with online electrochemical mass spectrometry. *Journal of The Electrochemical Society*, 163(6):A1095, 2016.

[20] Eui-Sun Hong, Shigeto Okada, Takaki Sonoda, S Gopukumar, and Jun-ichi Yamaki. Thermal stability of electrolytes with mixtures of lipf6 and libf4 used in lithium-ion cells. *Journal of the Electrochemical Society*, 151(11):A1836, 2004.

[21] Jiaxiang Zhang, Junwen Yang, Limin Yang, Hai Lu, Huan Liu, and Bin Zheng. Exploring the redox decomposition of ethylene carbonate–propylene carbonate in li-ion batteries. *Materials Advances*, 2(5):1747–1751, 2021.

[22] Zhenrong Lu, Li Yang, and Yaju Guo. Thermal behavior and decomposition kinetics of six electrolyte salts by thermal analysis. *Journal of power sources*, 156(2):555–559, 2006.

[23] Steven E Sloop, James K Pugh, John B Kerr, and Kim Kinoshita. Chemical reactivity of pf5 and lipf6 in ethylene carbonate/dimethyl carbonate. 2000.

[24] Chun Zhan, Tianpin Wu, Jun Lu, and Khalil Amine. Dissolution, migration, and deposition of transition metal ions in li-ion batteries exemplified by mn-based cathodes–a critical review. *Energy & Environmental Science*, 11(2):243–257, 2018.

[25] YiDi Zhang, Yi Li, XinHui Xia, XiuLi Wang, ChangDong Gu, and JiangPing Tu. High-energy cathode materials for li-ion batteries: A review of recent developments. *Science China Technological Sciences*, 58:1809–1828, 2015.

[26] Yang-Kook Sun. High-capacity layered cathodes for next-generation electric vehicles, 2019.

[27] David Schreiner, Tanja Zünd, Florian J Günter, Ludwig Kraft, Benedikt Stumper, Fabian Linsenmann, Michael Schüßler, Rebecca Wilhelm, Andreas Jossen, Gunther Reinhart, et al. Comparative evaluation of lmr-ncm and nca cathode active materials in multilayer lithium-ion pouch cells: Part i. production, electrode characterization, and formation. *Journal of The Electrochemical Society*, 168(3):030507, 2021.

[28] Geert Silversmit, Diederik Depla, Hilde Poelman, Guy B Marin, and Roger De Gryse. Determination of the v2p xps binding energies for different vanadium oxidation states (v5+ to v0+). *Journal of Electron Spectroscopy and Related Phenomena*, 135(2-3):167–175, 2004.

[29] Peng Liu. Vanadium-oxide-based electrode materials for li-ion batteries. 2017.

[30] Naoufal Bahlawane and Damien Lenoble. Vanadium oxide compounds: structure, properties, and growth from the gas phase. *Chemical Vapor Deposition*, 20(7-8-9):299–311, 2014.

[31] Samuel A Hevia, Joseba Orive, Fernando Guzmán, Eduardo Cisternas, Fabian Dietrich, Roberto Villarroel, and Judit Lisoni. High performance of v2o5 thin film electrodes for lithium-ion intercalation. *Applied Surface Science*, 576:151710, 2022.

[32] Songhee Choi, Jaeseok Son, Junhyeob Oh, Ji-Hyun Lee, Jae Hyuck Jang, and Shinbuhm Lee. Sharp contrast in the electrical and optical properties of vanadium wadsley (v m o 2 m+ 1, m> 1) epitaxial films selectively stabilized on (111)-oriented y-stabilized zr o 2. *Physical Review Materials*, 3(6):063401, 2019.

[33] Yujing Zhang, Ximiao Wang, Yang Zhou, Haojie Lai, Pengyi Liu, Huanjun Chen, Xiaomu Wang, and Weiguang Xie. Highly sensitive and ultra-broadband vo2 (b) photodetector dominated by bolometric effect. *Nano letters*, 22(1):485–493, 2021.

[34] Top Khac Le, Manil Kang, and Sok Won Kim. A review on the optical characterization of v2o5 micro-nanostructures. *Ceramics International*, 45(13):15781–15798, 2019.

[35] Yuwei Zhang, Yuting Luo, Cole Fincher, Sarbajit Banerjee, and Matt Pharr. Chemomechanical degradation in v 2 o 5 thin film cathodes of li-ion batteries during electrochemical cycling. *Journal of Materials Chemistry A*, 7(41):23922–23930, 2019.

[36] C Leger, S Bach, P Soudan, and J-P Pereira-Ramos. Structural and electrochemical properties of ω li x v 2 o 5 (0.4 x 3) as rechargeable cathodic material for lithium batteries. *Journal of The Electrochemical Society*, 152(1):A236, 2004.

[37] Bruno G Nicolau, Aaron Petronico, Kendra Letchworth-Weaver, Yasaman Ghadar,

Richard T Haasch, Julio ANT Soares, Ryan T Rooney, Maria KY Chan, Andrew A Gewirth, and Ralph G Nuzzo. Controlling interfacial properties of lithium-ion battery cathodes with alkylphosphonate self-assembled monolayers. *Advanced Materials Interfaces*, 5(10):1701292, 2018.

[38] Yan Zhuang, Yuqin Lei, Mingyun Guan, Fanghui Du, Haishang Cao, Hui Dai, Qun Zhou, Jason Adkins, and Junwei Zheng. 4-aminobenzoic acid as a novel electrolyte additive for improved electrochemical performance of li1. 2ni0. 2mn0. 6o2 cathodes via in situ electrochemical polymerization. *Electrochimica Acta*, 331:135465, 2020.

[39] Christian A Nijhuis, William F Reus, and George M Whitesides. Molecular rectification in metal- sam- metal oxide- metal junctions. *Journal of the American Chemical Society*, 131(49):17814–17827, 2009.

[40] Anapath electron-microscopy sem scheme. `https://anapath.ch/electron-microscopy-2/`. Accessed: 2023-10-19.

[41] Fred A Stevie and Carrie L Donley. Introduction to x-ray photoelectron spectroscopy. *Journal of Vacuum Science & Technology A: Vacuum, Surfaces, and Films*, 38(6):063204, 2020.

[42] Jean-Charles Arnault. X-ray photoemission spectroscopy applied to nanodiamonds: From surface chemistry to in situ reactivity. *Diamond and Related Materials*, 84:157–168, 2018.

[43] Fabian Dietrich, Juan Fernandez, Samuel Hevia, Eduardo Cisternas, and Marcos Flores. Determination of the conformational preference of para-aminobenzoic acid on vanadium pentoxide surface: An xps and dft study. *The Journal of Physical Chemistry C*, 125(37):20450–20459, 2021.

[44] Baohe Yuan, Xiang Yuan, Binger Zhang, Zheng An, Shijun Luo, and Lulu Chen. Lithium ion batteries cathode material: V2o5. *Chinese Physics B*, 31(3):038203, 2022.

[45] Heng-guo Wang, De-long Ma, Yun Huang, and Xin-bo Zhang. Electrospun v2o5 nanostructures with controllable morphology as high-performance cathode materials for lithium-ion batteries. *Chemistry–A European Journal*, 18(29):8987–8993, 2012.

[46] K Balogun, Precious Chukwunenye, Fatima Anwar, Ashwin Ganesan, Qasim Adesope, Dominic Willadsen, S Nemšák, Thomas R Cundari, Paul S Bagus, Francis D'Souza, et al. Interaction of molecular nitrogen with vanadium oxide in the absence and presence of water vapor at room temperature: Near-ambient pressure xps. *The Journal of Chemical Physics*, 157(10):104701, 2022.

[47] R Zimmermann, R Claessen, F Reinert, P Steiner, and S Hüfner. Strong hybridization in vanadium oxides: evidence from photoemission and absorption spectroscopy. *Journal of Physics: Condensed Matter*, 10(25):5697, 1998.

[48] J Mendialdua, R Casanova, and YJJOES Barbaux. Xps studies of v2o5, v6o13, vo2 and v2o3. *Journal of Electron Spectroscopy and Related Phenomena*, 71(3):249–261, 1995.

[49] ERALNE Hryha, Elin Rutqvist, and Lars Nyborg. Stoichiometric vanadium oxides studied by xps. *Surface and interface analysis*, 44(8):1022–1025, 2012.

[50] Rim Benali-Cherif, Radhwane Takouachet, E-E Bendeif, and Nourredine Benali-Cherif. The structural properties of a noncentrosymmetric polymorph of 4-aminobenzoic acid. *Acta Crystallographica Section C: Structural Chemistry*, 70(3):323–325, 2014.

[51] Kristin Persson. Materials Data on V_2O_5 (SG:59) by Materials Project, 11 2014.

[52] S Tougaard. Quases-imfp-tpp2m program. *Quases-Tougaard Inc*, 2016.

[53] Shigeo Tanuma, Cedric J Powell, and David R Penn. Calculations of electron inelastic mean free paths. v. data for 14 organic compounds over the 50–2000 ev range. *Surf. Interface Anal.*, 21(3):165–176, 1994.

[54] A. Jablonski, F. Salvat, C. J. Powell, and A. Y. Lee. *NIST Electron Elastic-Scattering Cross-Section Database Version 4.0.* NIST Standard Reference Database Number 64, National Institute of Standards and Technology, Gaithersburg MD, 20899, 2016. https://srdata.nist.gov/srd64/, (retrieved 23.04.2021).

[55] Grzegorz Greczynski and Lars Hultman. X-ray photoelectron spectroscopy: towards reliable binding energy referencing. *Progress in Materials Science*, 107:100591, 2020.

[56] Andrew G Thomas, Mark J Jackman, Michael Wagstaffe, Hanna Radtke, Karen Syres, Johan Adell, Anna Lévy, and Natalia Martsinovich. Adsorption studies of p-aminobenzoic acid on the anatase tio2 (101) surface. *Langmuir*, 30(41):12306–12314, 2014.

[57] Brian R Strohmeier. An esca method for determining the oxide thickness on aluminum alloys. *Surface and interface analysis*, 15(1):51–56, 1990.

[58] Anubhav Jain, Shyue Ping Ong, Geoffroy Hautier, Wei Chen, William Davidson Richards, Stephen Dacek, Shreyas Cholia, Dan Gunter, David Skinner, Gerbrand Ceder, et al. The materials project: A materials genome approach to accelerating materials innovation, apl mater. 2013.

[59] Cornel-Constantin Lalau, Anna Dimitrova, Marcel Himmerlich, Adriana Ispas, Tom Weier, Stefan Krischok, and Andreas Bund. An electrochemical and photoelectron spectroscopy study of a low temperature liquid metal battery based on an ionic liquid electrolyte. *Journal of the Electrochemical Society*, 163(10):A2488, 2016.

[60] Amey Nimkar, Netanel Shpigel, Fyodor Malchik, Shaul Bublil, Tianju Fan, Tirupathi Rao Penki, Merav Nadav Tsubery, and Doron Aurbach. Unraveling the role of fluorinated alkyl carbonate additives in improving cathode performance in sodium-ion batteries. *ACS Applied Materials & Interfaces*, 13(39):46478–46487, 2021.

[61] Jangho Park, Sanghyuk Park, Mincheol Beak, Seongdeock Jeong, and Kyungjung Kwon. Impacts of residual electrolyte components of spent lithium-ion batteries on the physical/electrochemical properties of resynthesized cathode active materials. *Journal of*

Cleaner Production, 379:134570, 2022.